Cylindrical Optical Dipole Trap for Ultracold Atoms

Anders Ploug Hansen
Student number: 201607909
Department of Physics and Astronomy
Aarhus University, Denmark

Supervisor: Jan Joachim Arlt

Master's Thesis
June 16, 2021

ABSTRACT

Ultracold atomic gases have been the subject of intense experimental and theoretical interest for the past 25 years and have allowed for investigations of the quantum properties of matter. Accumulation of ultracold atoms in a single quantum state, known as a Bose-Einstein condensate, has opened the door for several research avenues in the pursuit of understanding complicated quantum systems. A quantum system consisting of an impurity interacting with a surrounding medium, where the interaction strength can be tuned using magnetic fields, is one example of ongoing investigations. The results of such an investigation heavily rely on the methods for storage and trapping of atoms and typically is it desirable to use optical trapping potentials to confine the atoms.

This thesis presents the experimental realization of a blue-detuned ring beam that can be used as a repulsive optical dipole potential. Due to the design of the trap, which involves three axicons, a box potential with steep inner walls is demonstrated, allowing for a homogeneous distribution of atoms inside the trap. Two setups with different combinations of lenses and axicons are characterized and compared, based on laboratory results and ray tracing simulations. Finally, an imaging system used to project the ring onto the atoms is presented.

The experimental product of this thesis will serve as an extension to the current experimental apparatus used in MIX lab at Aarhus University, with the goal of replacing the current attractive crossed dipole trap. Thus, it will contribute to improving results in the study of impurity dynamics in Bose-Einstein condensates.

RESUMÉ

DANISH ABSTRACT

Ultrakolde atomare gasser har været et emne med intens eksperimentel og teoretisk interesse de sidste 25 år, og har tilladt undersøgelser af kvantemekaniske egenskaber af stof. Ophobning af ultrakolde atomer i en enkelt kvantetilstand, kendt som et Bose-Einstein kondensat, har åbnet døren for adskillige forskningsveje i forfølgelsen for at forstå komplicerede kvantesystemer. Et kvantesystem bestående af en urenhed der interagerer med det omkringliggende miljø, hvor interaktionsstyrken kan blive reguleret ved brug af magnetfelter, er et eksempel på igangværende undersøgelser. Et sådant studie afhænger kraftigt af metoderne brugt til at opbevare og fange atomer, og typisk er det ønskeligt at have optiske fældepotentialer til at begænse atomerne.

Denne afhandling præsenterer en eksperimentel realisering af en blå-detuned ring stråle der kan blive brugt som en frastødende optisk dipolpotential. Grundet designet af fælden, som involverer tre axicons, så vil et box potentiale med stejle indre mure blive demonstreret, som vil kunne tillade en homogen fordeling af atomer inde i fælden. To opstillinger med forskellige kombinationer af linser og axicons karakteriseres og sammenlignes, baseret på laboratorieresultater og ray-tracing simuleringer. Til sidst vil et billeddannelsessystem, brugt til at projicere ringen ned på atomerne, blive præsenteret.

Det eksperimentelle produkt af denne afhandling vil tjene som en udvidelse til det nuværende eksperimentelle apparatur brugt i MIX lab på Aarhus universitet, med målet om at erstatte den nuværende attraktive krydsende dipolfælde. Dermed vil det bidrage til at forbedre resultater i forbindelse med studiet af urenheds dynamik i Bose-Einstein kondensater.

PREFACE

This thesis constitutes 45 ECTS-points and is made in completion of the master's education in Physics at the Department of Physics and Astronomy, Aarhus University. The experimental work was carried out in a preparation lab, which is part of the Multi Species Quantum Gases Experiment.

I would like to use this opportunity to thank some of the people that have been involved in my work for the past year. First, a big thanks to my supervisor Jan Arlt for his friendly guidance and great lectures on BECs during my time in the group. Then I would like to thank Magnus Graf Skou and Thomas Guldager Skov for teaching me about the experimental apparatus in MIX lab, and for always taking the time to help me with experimental equipment, theory discussion etc. Shortly after I started on my thesis, Andreas Madsen Morgen started as a new Ph.D. student in the group, whom I would like to thank for kindly providing the GPELab simulations presented in this thesis. Lastly, I would like to thank Andreas Madsen Morgen, Jan Arlt and Carrie Ann Weidner for proofreading the thesis.

Anders Ploug Hansen

CONTENTS

CHAPTER 1

INTRODUCTION

At the beginning of the 20th century, the theory of quantum mechanics started to emerge and paved the way for what we now consider to be a central part of modern physics. Although it was hard to accept, to begin with, because of its non-intuitive way of thinking compared to classical physics, it is today considered to be one of the most successful theories ever formulated, if not the most successful. The sovereignty of quantum mechanics comes to light when studying systems at the atomic- and subatomic level. However, macroscopic manifestations of quantum effects, e.g. superconductivity [1] and the quantum Hall effect [2], can be directly observed on much larger length scales.

It can often be challenging to investigate quantum effects since it requires a model system where the experimental parameters can be carefully controlled. Nevertheless, it is possible to construct such systems, and ultracold atomic gases are excellent candidates to fulfill this requirement. When a dilute cloud of atoms is cooled below a certain threshold temperature, the cloud itself undergoes a phase-transition where a majority of the atoms occupy the lowest possible quantum state. When this happens, one has created a Bose-Einstein Condensate (BEC). Ultracold atoms and in particular BECs have been a subject of interest for about a century. The first predictions of BECs were made in 1924-1925 by Albert Einstein [3] following the pioneering work done by Satyendra Nath Bose on Bose statistics [4]. Because of the extremely low temperature requirement for a BEC to form, i.e. around a few hundred nanokelvin, experimental realizations have not been demonstrated until fairly recently. In 1995 it was demonstrated by Anderson et al.[5] that a BEC of rubidium-87 atoms can be attained using first laser cooling and then magnetic fields together with evaporative cooling. This procedure of cooling bosons has been the go-to method ever since to reach temperature in the micro kelvin region.

A lot of research has been conducted to investigate the properties of a BEC. This has led to the experimental observation of superfluidity through the formation of vortices by stirring the BEC with lasers [6]. Coherence is another important property that can be observed when two clouds of condensed Bose atoms start to overlap, thus creating an interference pattern where fundamental concepts of wave-like behavior can be studied [7, 8]. A particularly hot topic at the moment, here at Aarhus University (AU), is impurity dynamics. When an impurity is immersed in a BEC, the interaction between the BEC and the impurity can lead to the formation of quasiparticles termed Bose polarons [9], and bipolarons in the case where two polarons interact with each other [10].

The main obstacle, related to the ongoing investigations of the Bose polaron here at AU, is connected to the experimental apparatus being used. In the current setup (described in [11]), a red-detuned optical dipole trap is used to confine the atoms. The generated potential arising from such a trap is harmonic, resulting in an inhomogeneous density of the BEC. The non-uniform density leads to spatially varying energies which prevent researchers from probing local properties of strongly interacting many-body systems. In particular, the spectroscopic signal from the Bose polaron depends on the local density in the trap, thus a harmonic trap leads to broadening effects in the energy spectrum of the polaron [12].

One way to circumvent this issue is to make a trapping potential that yields a single density across the trap. In other words, one needs a potential with a flat bottom. The textbook example of such a potential is the square well characterized by the barriers that confine the particle. In the finite well, there is a non-zero probability for the particle to be found outside of the well, even though the potential barrier is higher than the total energy of the particle. This is another example of a quantum effect known as tunneling. To design a trap that possesses box-like properties we thus need not only high repulsive walls to prevent quantum tunneling, but we also need steep walls in order to achieve a uniform particle distribution.

So far this has been realized in a number of laboratories. Common for all setups is the use of a blue-detuned laser such that the atoms are repelled from the region of high light intensity, instead of attracted like in the red-detuned case. In Gaunt et al.[13] the trap consists of a hollow tube beam for radial confinement and two sheet beams for axial confinement and thus realizes a cylindrical potential for the atoms. The three trapping beams are created by reflecting a single Gaussian beam off a phase-imprinting spatial light modulator (SLM). In Mukherjee et al. [14] a special type of lens called an axicon is used, which alters the geometry of the incoming Gaussian beam by transforming it into a ring-shaped beam. To block any undesirable light generated within the ring, an opaque mask is inserted. This also offers three-dimensional confinement where the atoms are trapped in the radial direction by the cylinder-shaped beam and the end caps are created by another laser focused onto the edges of a rectangular opaque mask. Finally, Hueck et al. [15] use a similar setup but without introducing an opaque mask. To block the residual light inside the ring generated by the axicon, they instead use a combination of a lens and two additional axicons to produce a hollow cylindrical beam.

Within this thesis, a setup similar to the latter is described, constructed and characterized in detail.

1.1 Thesis outline

Chapter 2: Ultracold quantum gases
Some of the key concepts important for ultracold quantum gases are explored. This includes Bose-Einstein condensation in the non-interacting and interacting case alongside an introduction to Feshbach resonances. Then the optical dipole potential is presented before the chapter is concluded with a consideration of the effect of gravity in optical dipole traps.

Chapter 3: Optical Box Potential
A detailed description of the experimental setup to create a hollow ring is given in this chapter. This includes a discussion of the distances between some of the optical elements, and how they impact the size and shape of the ring, based on results from ray tracing simulations.

Chapter 4: Cylindrical Box characterization
This chapter presents the key characteristics of the ring potential for two different setups. It also presents the imaging system used to project the ring onto the atoms.

Chapter 5: Conclusion and outlook
The thesis concludes with a summary of the key results obtained and an outlook for future work.

CHAPTER 2

ULTRACOLD QUANTUM GASES

The focus of this chapter provides the theoretical background related to the creation and confinement of Bose-Einstein condensates. In Sec. 2.1 a basic introduction to BECs is given, by first looking at the condensation of non-interacting bosons and then include inter-atomic interactions inside a BEC where the Gross-Pitaevskii (GP) equation is introduced. This is followed by a subsection where the GP equation is solved numerically in two different trapping potentials, harmonic- and box potential, to study how the density distribution changes for different numbers of ^{39}K atoms in the two types of external potentials. It is then shown how the interaction between different quantum states can be tuned arbitrarily using the so-called Feshbach resonances presented in Sec. 2.2. The optical dipole potential that is the confining potential for an optical dipole trap (ODT), will be derived in Sec. 2.3. Finally, the chapter is concluded by Sec. 2.4 where the effect of gravity in an ODT is considered.

2.1 Bose-Einstein Condensation

The behavior of integer spin particles called bosons have been extensively investigated ever since the description of Bose-statistics was first considered back in 1924 by Bose. First massless particles like photons were treated in the framework of Bose-statistics, and shortly after Einstein applied it to particles of mass. An interesting prediction came out when a system of massive bosons was studied at extremely low temperatures, namely that the system would condensate into what is thought of as a fifth state of matter and today known as a Bose-Einstein Condensate (BEC).

2.1.1 Condensation of an ideal bosonic gas

In a system of bosonic particles where the temperature T is well above absolute zero and quantum effects are negligible, Maxwell-Boltzmann statistics can be applied. The expected number of particles in a state with energy ϵ_i is then given by

$$f(\epsilon_i) = \frac{1}{e^{(\epsilon_i - \mu)/k_B T}},$$

where k_B is the Boltzmann constant and μ is the chemical potential. As we start to approach absolute zero, the mean occupancy in each quantum state tends to rise and quantum statistics are needed. This starts to happen when the de Broglie wavelength becomes comparable with the inter-particle distance where the particles can no longer be distinguished from each other. For such a system of non-interacting bosons the average occupancy of a given state will then be given by the Bose-Einstein distribution

$$f(\epsilon_i) = \frac{1}{e^{(\epsilon_i - \mu)/k_B T} - 1}. \tag{2.1}$$

To find the total number of particles N in the system, one must sum over all possible quantum states. As the temperature is lowered even further, i.e. below a critical value T_C, there will be a macroscopic occupation of the lowest single-particle state and a BEC has been achieved. Thus, we have that $N_0/N > 0$ for $N \to \infty$ where N_0 is the number of particles we have in the BEC. The transition temperature T_C will ultimately depend on the trap at which the system is confined, and can be expressed as [16]

$$k_B T_C = \frac{N^{1/\alpha}}{[C_\alpha \Gamma(\alpha)\zeta(\alpha)]^{1/\alpha}}, \tag{2.2}$$

where C_α is a constant, $\Gamma(\alpha)$ is the gamma function and $\zeta(\alpha)$ is the Riemann zeta function. The parameter α which appears in every factor in Eq. (2.2) is trap dependent. For a 3D gas confined by rigid walls (box potential), α is equal to $3/2$ and the constant C_α is related to the density of states. Thus for a uniform Bose gas, which is a consequence of a box potential, the critical temperature will be given by

$$k_B T_C \approx 3.31 \frac{\hbar n^{2/3}}{m}, \tag{2.3}$$

where $\hbar$ is the reduced Planck constant, n is the number density and m is the mass of the particle. A similar expression exists for the 3D harmonic oscillator potential given by

$$k_B T_C \approx 0.94 \hbar \bar{\omega} N^{1/3}, \tag{2.4}$$

where $\bar{\omega}$ is the geometric mean of the three oscillator frequencies. Finally, both Eq. (2.3) and (2.4) can be related to the condensate fraction by the following formula

$$\frac{N_0}{N} = \left[1 - \left(\frac{T}{T_C}\right)^{\alpha}\right], \tag{2.5}$$

where $\alpha = 3$ for the 3D harmonic oscillator potential, and $\alpha = 3/2$ for the box potential. It is important to note that the value of T_C does not depend on the interaction between the particles, which testify that BECs are a direct consequence of quantum statistics.

2.1.2 The Gross-Pitaevskii equation

In the previous section, we presented one of the key predictions from Bose-Einstein statistics leading up to the macroscopic quantum phenomenon of BECs. This was done entirely without the consideration of inter-atomic interactions. In real experiments, interactions between particles are of course present and should not be swept under the rug. Although as we will see in Sec. 2.2, it is possible to tune the interaction strength to be zero, nevertheless interactions are still needed in order to reach thermal equilibrium. The total Hamiltonian describing a gas of N interacting atoms is given by

$$\hat{H} = \sum_{i=1}^{N}\left[-\frac{\hbar^2}{2m}\nabla_i^2 + V_{\text{trap}}(\mathbf{r}_i)\right] + \sum_{i,j}^{N} V_2(\mathbf{r}_i,\mathbf{r}_j) + \sum_{i,j,k}^{N} V_3(\mathbf{r}_i,\mathbf{r}_j,\mathbf{r}_k) + \ldots \tag{2.6}$$

The first term is the well-known single-particle kinetic energy term, V_{trap} is the external potential due to the confining trap, and the remaining terms are the interatomic potentials due to the two-body interaction, V_2, three-body interaction, V_3, and so on. In general, a Hamiltonian of this sort can be very challenging to work with thanks to the interaction terms, and therefore assumptions must be made without losing the ability to describe the properties of the quantum system. One way to treat this problem is by going with a mean-field approach, where the many-body problem reduces to a much simpler two-body problem. The central assumption will be, that we are working with a dilute cloud at zero temperature, thus the interaction is weak and therefore short-ranged. Collisions of three and more particles will under this assumption be highly unlikely and can therefore be neglected. The two-body interaction potential V_2 can then be modelled as a simple contact interaction $U_0\delta(\mathbf{r}-\mathbf{r}')$, where $\mathbf{r}$ and $\mathbf{r}'$ are the positions of the two atoms and $U_0 = 4\pi a/m$ where a is the s-wave scattering length and m is the atom mass. Because we have $T = 0$ all the bosons are condensed into the same single particle state $\phi(\mathbf{r})$. Thus it is fair to assume that the wave function of this N-particle system can be written as a symmetrized product of single-particle wave functions

$$\Psi(\mathbf{r}_1, \mathbf{r}_2, ..., \mathbf{r}_N) = \prod_{i=1}^{N} \phi(\mathbf{r}_i), \tag{2.7}$$

each having the usual normalization condition

$$\int d^3r |\phi(\mathbf{r})|^2 = 1. \tag{2.8}$$

From this the total density of the gas must then be $n(\mathbf{r}) = N|\phi(\mathbf{r})|^2$, or if we introduce the condensate wave function by $\psi(\mathbf{r}) = N^{1/2}\phi(\mathbf{r})$ the density of the gas can be expressed as $n(\mathbf{r}) = |\psi(\mathbf{r})|^2$. By taking the expectation value in this state of the simplified version of Eq. (2.6) where terms higher than the two-body interactions are excluded one can get an expression for the energy of the gas. Mean-field theory tells us that this energy should be minimized with respect to $\psi(\mathbf{r})$. A thorough description of this step can be found in [16], and the outcome is the Gross-Pitaevskii (GP) equation given by

$$-\frac{\hbar^2}{2m}\nabla^2\psi(\mathbf{r}) + V_{\text{trap}}(\mathbf{r})\psi(\mathbf{r}) + U_0|\psi(\mathbf{r})|^2\psi(\mathbf{r}) = \mu\psi(\mathbf{r}). \tag{2.9}$$

The GP equation is very much familiar with the Schrödinger equation, the difference lies in the third non-linear term in (2.9), but also in the corresponding eigenvalue of the system. In the GP equation the chemical potential, μ, is the eigenvalue and not the energy per particle.

For most ultracold systems where the number of atoms in the condensate is large, the kinetic energy term in Eq. (2.9) can be neglected under the so-called Thomas-Fermi approximation. The density of the cloud is then given by a rather simple expression

$$n(\mathbf{r}) = |\psi(\mathbf{r})|^2 = \frac{\mu - V_{\text{trap}}(\mathbf{r})}{U_0}, \tag{2.10}$$

which for a harmonic trap will result in an inverted parabolic density profile. However, this approximation fails near the edges of the cloud and would yield a physically unrealistic sharp edge at the surface [17]. To characterize the typical length scale at which the wave function can change, one can equate the kinetic energy term to the energy scale given by the chemical potential. From Eq. (2.10) it can be seen, that for a uniform Bose gas the chemical potential will simply be equal to $\mu = U_0 n(\mathbf{r})$, thus the characteristic length scale, ξ, at which the wave function varies, can be found to be

$$\frac{\hbar^2}{2m\xi^2} = U_0 n \qquad \Rightarrow \qquad \xi = \sqrt{\frac{\hbar^2}{2mnU_0}}. \tag{2.11}$$

This length scale is known as the *healing length* since it describes the distance over which the condensate density grows from zero to n. For a repulsive ODT where the walls are not modelled as infinitely hard, the healing length is related to the steepness of the potential that the atoms feel. It also provides the typical size of the core of a vortex when studying superfluid effects [6].

2.1.3 GPELab simulations

Now that we have established the GP-equation, which we saw as the governing equation describing the ground state of a quantum system of identical bosons, it would be interesting to simulate how the wave function or rather the density of the cloud takes shape in various potentials. This is where GPELab [18], which is a MATLAB toolbox, comes in handy. GPELab is designed to solve the GP-equation by applying different numerical techniques including the Spectral scheme (See [19] for an in-depth description of the algorithms being used). The resolution of the simulations depends on the number of grid points you choose, where the computation time of course rises if the number of grid points increases.

Other input parameters would be the scattering length, a, between the atoms, the number of atoms and the characteristic trap length which are all used in defining the non-linear interaction term in Eq. (2.9). Finally, the external potential must also be provided, before the ground state wave function of the BEC is extracted from the program.

The following simulations were kindly provided by Andreas M. Morgen who is a ph.D. student in the group. All the simulations are produced with a constant scattering length of $a = 100a_0$ with a_0 being the Bohr radius. The first round of simulations shows the density of the cloud along the x-axis of the system for different atom numbers in an isotropic harmonic oscillator potential, shown in figure 2.1. The characteristic trap length for this potential is given by the harmonic oscillator length $a_{ho} = \sqrt{\hbar/(m\omega)}$ which the x-axis is scaled with. It is clear, as we increase the number of atoms in the trap, the density distribution starts to deviate from the ideal gas described by a Gaussian distribution, and approaches the Thomas-Fermi regime where the condensate resembles that of an inverted parabolic distribution. Although the atoms are drawn towards the middle of the trap where the potential is lowest, mutual repulsive interactions, due to the positive scattering length, prevents the atoms from piling up at the center.

A more suitable potential for this project, which is also relatively easy to simulate, is the box potential where the walls are set to be infinitely high and steep. The wave function for an ideal gas along the x-axis in a box potential is given by [20]

$$\Psi_n(x) = \sqrt{\frac{2}{A_x}} \sin\left(\frac{n\pi}{A_x} x\right), \tag{2.12}$$

where A_x is the box length in the x-direction and n is an integer number with $n = 1$ corresponding to the ground state. The modulus squared of Eq. (2.12) alongside the GPELab simulations are plotted in figure 2.2 for the same different atom numbers as in the harmonic oscillator case

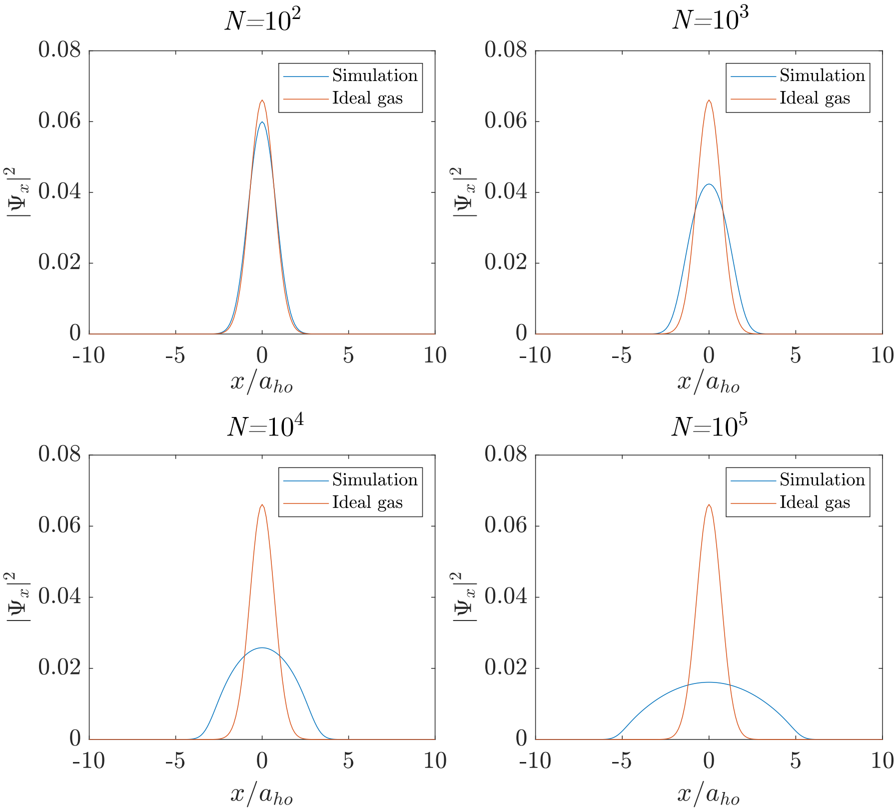

Figure 2.1: GPELab simulations of N-particles in an isotropic harmonic oscillator potential (blue curve). The non-interacting ideal gas described by a Gaussian function is also plotted (orange curve).

except that $N = 100$ is substituted with $N = 10^6$. The simulations are executed with a box length of $A = 80\,\mu\text{m}$. The x-axis is scaled with the characteristic trap length which is $L_{\text{trap}} = 10\,\mu\text{m}$. A parallel can be drawn between the box potential and the harmonic potential; As we increase the number of atoms in our trap, the distribution tends to flatten out due to the repulsive interaction between the atoms. Only this time, the atoms do not feel the force from the external trapping potential until they reach the boundaries of the trap. This is what creates the uniform and homogeneous distribution of an atom sample in a box trap. As the plateau in the density distribution gets broader, due to increasing atom numbers, the healing length introduced in Eq. (2.11) gets shorter.

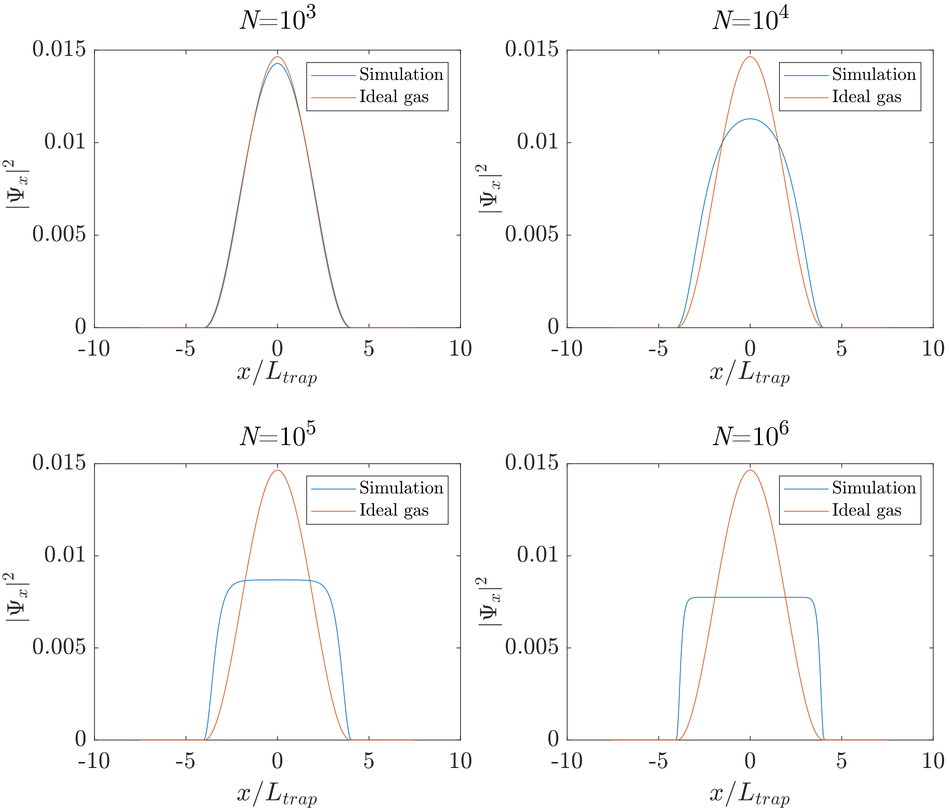

Figure 2.2: GPELab simulations of N-particles in a box potential with infinite high- and steep walls (blue curve). The non-interacting ideal gas described by the modulus squared of Eq. (2.12) is also plotted (orange curve). In the bottom plots, a plateau of constant density is visible.

2.2 Feshbach Resonances

Modern investigations of ultracold atomic gases heavily rely on the extraordinary degree of control that such a system has to offer under various conditions. This is not only limited to atomic and molecular physics but is also seen in other fields such as condensed matter, few- and many-body physics. The essential tool for controlling is the so-called Feshbach resonances, which is used to precisely tune the interaction between atomic states in the system, e.g. by applying an external magnetic field. Not all atomic species possess these resonances, but alkali atoms in particular like ^{39}K have been studied widely [21] when cooled to low temperatures where few channels are open. A direct benefit of having low temperatures is that one can describe the collisions between atoms in the low energy regime. Assuming elastic scattering and applying the formalism of a partial wave expansion one will only see contributions from the s-wave to the lowest order. The cross-section σ of such a scattering event can be written as

$$\lim_{k\to 0} \sigma = 4\pi a^2, \tag{2.13}$$

where a is known as the scattering length which can be thought of as a length at which two atoms see each other. Note that this equation is only true in the limit where the wavenumber k goes towards zero (low energies). For a two-body collision between particle A and particle B, we can have both open- and closed channel potentials. The open channel can be considered energetically accessible while the closed channel is forbidden by energy conservation. The closed channel can e.g. be thought of as a bound molecular state while the open channel is the background potential that connects the two atoms. If the energy of the bound molecular state is equal to the incoming particle energy, the collision process between the two particles is said to be on “resonance”. In the case of an ultracold atom system the atom-atom interaction is caused by the hyperfine interaction which flips the electronic and nuclear spins of one of the colliding atoms [22]. This interaction can then be tuned magnetically, by exploiting the Zeeman effect on the hyperfine states or by optical methods where the Stark effect is present. In the vicinity of a magnetically tuned Feshbach resonance, the scattering length can be expressed as [23]

$$a(B) = a_{bg}\left(1 - \frac{\Delta}{B - B_0}\right), \tag{2.14}$$

where Δ is the width of a given resonance, B_0 is the field at the center of the resonance, and a_{bg} is the background scattering length, i.e. the scattering length far away from resonance. From Eq. (2.14) it is evident that both positive and negative scattering lengths can be achieved corresponding to repulsive and attractive interactions, respectively.

In this thesis, a particular Feshbach resonance for the $4^2\mathrm{S}_{1/2}$ ground state of ^{39}K is of interest. The interaction between the $|F = 1, m_F = -1\rangle$ and $|F = 1, m_F = 0\rangle$ state has a resonance located at around 526 G. This is shown as the red line in figure 2.3. It is worth mentioning that using a magnetic field in the vicinity of 526 G will in practice only vary the interaction strength of the $|1, 0\rangle + |1, -1\rangle$ coupling while the two other internal interaction strengths will be held constant. Why this particular Feshbach resonance is chosen will be explained in Sec. 2.4.2.

2.3 Optical dipole Potentials

Optical trapping potentials have proofed to be excellent tools, especially when studying impurity dynamics where the magnetic field is needed as a free parameter, to tune the scattering length in the vicinity of a Feshbach resonance. This is the main reason why magnetic traps cannot be used: the effective interaction around the resonance is a strong function of the magnetic field. It is therefore desirable that the magnetic field is homogeneous, thus ruling out the possibility of magnetic traps.

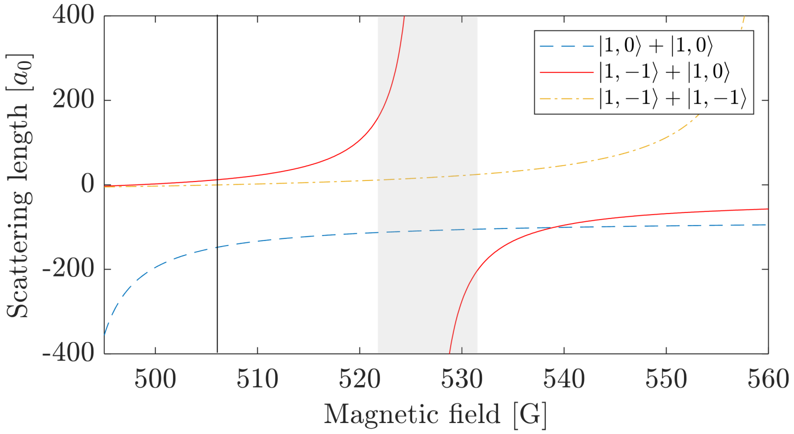

Figure 2.3: Scattering length as a function of applied magnetic field for interactions within the same hyperfine state $F = 1$ but for different m_F-states. The Feshbach resonance is present at 526 G for the interaction between the $|F = 1, m_F = 0\rangle$ state and the $|F = 1, m_F = -1\rangle$ state (red line). The two internal interactions of $|1,0\rangle$ and $|1,-1\rangle$ is also shown (dashed blue- and dot-dashed yellow line respectively). The black vertical line at around 506 G indicates the zero crossing for the condensate state $|1,-1\rangle$. The gray shaded area shows the interesting region at which impurity dynamics can be studied.

Generally, one distinguishes between two overall types of optical traps: charged- and neutral particle traps. For charged particles, one wants to exploit the Coulomb interactions between the atoms and the external electric or electromagnetic fields. This kind of trap is known as an ion trap and can for instance be used to study entangled states of trapped atomic ions [24]. The other type which is the relevant one for this project is a trap that can be used to confine neutral atoms. The trapping mechanism for neutral particles is much weaker than the Coulomb interaction in the charged particle case. Therefore, one would need a precooled atom sample in the microkelvin region for the neutral atom traps to work. The operation of optical dipole traps relies on the electric dipole interaction with far-detuned light from the atomic transitions. If one was to operate the trap close to resonance, one would have a radiation pressure trap that possess other characteristics. The effects of light on atoms, and more specifically the dipole potential that will be presented in this section, will be based on the theory described in [25] and [26]. When a neutral atom is placed in the presence of light, could be a monochromatic light source like a laser, an induced dipole moment arises in the atom, due to the electric field **E** of the light, that oscillates at the driving frequency ω. The induced dipole moment will be given by $\mathbf{p} = \alpha\mathbf{E}$, where α is defined as the complex polarizability which describes how easily the field induces the dipole moment **p**. In other words, it characterizes the response of the atom to the applied field. The real part of α is related to the dipole force and thus the potential energy, while the imaginary part is related to the absorption and rescattering of the incident light. From a classical point of view the interaction potential, due to the induced dipole moment, is then given by

$$U_{\mathrm{dip}} = -\frac{1}{2}\langle \mathbf{pE} \rangle = -\frac{1}{2\epsilon_0 c}\mathrm{Re}(\alpha) I(\mathbf{r}). \tag{2.15}$$

Because the dipole moment is induced, the factor of 1/2 appears which is not usually present for the dipole energy. If the dipole energy was to be written out explicitly, there would be terms that oscillate too fast for the atoms to respond, and therefore these terms can be omitted by taking the time average, which is denoted by the angular brackets. The field intensity I is given by $I = 2\epsilon_0 c|E_0|^2$, where E_0 is the field amplitude. Since the dipole force can be considered conservative, the force can be derived from the dipole potential simply by taking the gradient of U_{dip}

$$\mathbf{F}_{\mathrm{dip}}(\mathbf{r}) = -\nabla U_{\mathrm{dip}}(\mathbf{r}) = \frac{1}{2\epsilon_0 c}\mathrm{Re}(\alpha)\nabla I(\mathbf{r}). \tag{2.16}$$

Thus we see that the dipole force is proportional to the real part of the polarizability and the intensity gradient. The power extracted by the induced dipole moment can be written as

$$P = \langle \dot{\mathbf{p}}\mathbf{E} \rangle = \frac{\omega}{\epsilon_0 c}\mathrm{Im}(\alpha)I(\mathbf{r}), \tag{2.17}$$

and will be re-emitted as dipole radiation. If we consider the light to be a stream of photons each with energy $\hbar\omega$ we can interpret the scattering rate simply as the absorbed power divided by the photon energy

$$\Gamma_{\mathrm{sc}} = \frac{P}{\hbar\omega} = \frac{1}{\hbar\epsilon_0 c}\mathrm{Im}(\alpha)I(\mathbf{r}), \tag{2.18}$$

one can see this scattering of photons as a source of heat generation in the cloud of atoms.

The classical way to obtain an expression for the polarizability would be to consider the atom in the Lorentz model, i.e. treat the electron as a damped harmonic oscillator where the equation of motion is given by

$$m_e\ddot{\mathbf{x}} + m_e\Gamma\dot{\mathbf{x}} + m\omega_0^2\mathbf{x} = -e\mathbf{E}(t). \tag{2.19}$$

Here $\mathbf{E}(t) = \hat{\epsilon}E_0e^{-i\omega t}$ and the damping term $m_e\Gamma\dot{\mathbf{x}}$ can be interpreted as the classical analog of spontaneous emission and collisions with other atoms. By having an ansatz on the form

$$\mathbf{x}(t) = \hat{\epsilon}x_0e^{-i\omega t}, \tag{2.20}$$

the solution to Eq. (2.19) can be shown to be

$$x_0 = \frac{eE_0/m}{\omega^2 - \omega_0^2 + i\Gamma\omega}. \tag{2.21}$$

Now recall that the definition of the dipole moment is given by

$$\mathbf{p} = e\mathbf{x} = \alpha(\omega)\mathbf{E}. \tag{2.22}$$

From this we have derived an expression for the polarizability

$$\alpha(\omega) = \frac{e^2/m}{\omega^2 - \omega_0^2 + i\Gamma\omega}, \tag{2.23}$$

where Γ is the classical damping rate due to the radiative energy loss given by

$$\Gamma = \frac{e^2\omega^2}{6\pi\epsilon_0 m_e c^3}. \tag{2.24}$$

It is worth noting that although this derivation is done all classically, it still has great precision when calculated on to specific atoms which have strong dipole allowed transitions. For alkali atoms, which are characterized by only having one valence electron, Eq. (2.24) tend to agree with the true decay rate to within a few percent [25].
A more general approach is to do it semi-classically where we treat the atom as a two-level quantum system, having a ground state and an excited state, interacting with a classical light field. Here the damping rate would depend on the dipole matrix element as follows

$$\Gamma = \frac{\omega_0^2}{3\pi\epsilon_0\hbar c^3}\left|\langle e|\mathbf{p}\cdot\hat{\epsilon}|g\rangle\right|^2, \tag{2.25}$$

where $|g\rangle$ is the ground state and $|e\rangle$ is the excited state of the atom. If saturation effect can be neglected, i.e. if the occupation level in the excited state is negligible, then Eq. (2.24) will be sufficient. This can be fulfilled by having a dipole trap driven far away from resonance, i.e. having a laser system that is far-detuned such that the scattering rate is much lower than the spontaneous decay rate ($\Gamma_{\mathrm{sc}} \ll \Gamma$). We are now in a position where we can write Eq. (2.15) and (2.18) more explicitly by using the derived expression of the polarizability in equation (2.23) to get:

$$
\begin{aligned}
U_{\mathrm{dip}}(\mathbf{r}) &= -\frac{3\pi c^2}{2\omega_0^3}\left(\frac{\Gamma}{\omega_0-\omega}+\frac{\Gamma}{\omega_0+\omega}\right) I(\mathbf{r}),\\
\Gamma_{\mathrm{sc}}(\mathbf{r}) &= \frac{3\pi c^2}{2\hbar\omega_0^3}\left(\frac{\omega}{\omega_0}\right)^3\left(\frac{\Gamma}{\omega_0-\omega}+\frac{\Gamma}{\omega_0+\omega}\right)^2 I(\mathbf{r}),
\end{aligned}
$$

which are valid approximations as long as the detuning is large and saturation effects are negligible. Further approximations can be made if the detuning of the light $\delta = \omega - \omega_0$ is not too large ($|\delta| \ll \omega_0$). In this way, the so-called counter-rotating term $\Gamma/(\omega_0+\omega)$ can be neglected since $\omega/\omega_0 \approx 1$. This approximation is known as the rotating-wave approximation and the above expressions will be simplified to:

$$U_{\mathrm{dip}}(\mathbf{r}) = \frac{3\pi c^2}{2\omega_0^3}\left(\frac{\Gamma}{\delta}\right) I(\mathbf{r}), \tag{2.26}$$

$$\Gamma_{\mathrm{sc}}(\mathbf{r}) = \frac{3\pi c^2}{2\hbar\omega_0^3}\left(\frac{\Gamma}{\delta}\right)^2 I(\mathbf{r}). \tag{2.27}$$

It can be seen directly from Eq. (2.26), that depending on which detuning we are operating the dipole trap at, we have either an attractive or repulsive interaction between the atoms and the electric field. If the detuning is negative ($\delta < 0$) compared to an atomic transition the interaction can be considered attractive, i.e. atoms are drawn towards regions of higher intensity, and we call it a red detuned trap. On the contrary, if the detuning is positive, ($\delta > 0$) the dipole interaction is repelling and atoms will move towards regions of lower intensity, which we call a blue detuned trap. Experimentalists will face a trade-off in the desire of having a deep trap together with a low scattering rate. However, since the potential scales as I/δ while the scattering rate scales as I/δ^2, optical dipole traps are preferably operated at high intensities and large detunings to keep the scattering rate as low as possible.

2.4 Gravitational Potential Compensation

The ideal testbed for an optical dipole trap would be in an environment where no external forces are present, and where the atoms in the trap only are repelled by the optical dipole force that arises between the atoms and the blue detuned laser. However, in reality where experiments are conducted on earth, there will always be an external force acting on the atoms due to the presence of the earth's gravitational field. This will lead to undesired effects in experiments and thus limits the size, shape and density of the trapped atomic cloud. Nonetheless, it is possible to compensate for this gravitational potential by turning the attention to magnetic fields because the atomic states are magnetically sensitive.

The section is structured as follows. First a brief look at the theory of the Zeeman splitting of hyperfine states and the introduction of the Breit-Rabi formula which describes the energy splitting at different magnetic field strengths. Then we will go on to look at the energy splitting of the $4^2\mathrm{S}_{1/2}$ ground state of ^{39}K and in particular, investigate the $|F=1, m_F=-1\rangle$ and $|F=1, m_F=0\rangle$ behavior in different magnetic field regime, before we finally will be able to calculate the necessary magnetic field gradient needed to compensate for the gravitational potential at the Feshbach resonance close to 526 G mentioned in section 2.2.

2.4.1 Zeeman splitting of hyperfine manifold

The Zeeman effect is the splitting of energy levels into sub-levels due to the atoms magnetic moment interacting with an external magnetic field. In the hyperfine case where F is a good quantum number, we have $2F+1$ magnetic sub-levels labelled by the quantum number m_F. These sub-levels will be degenerate in the absence of an external magnetic field. However, in the presence of a magnetic field the Zeeman splitting of the hyperfine manifold can be described in 3 regimes; the low-, intermediate- and high magnetic field regimes.

In the case where the hyperfine energy splitting is greater than the atom's interaction with the external magnetic field, the interaction Hamiltonian will only slightly perturb the hyperfine Hamiltonian, and the resulting energy splitting can be described by a simple linear relation. This is given by [17]

$$\Delta E_Z = \mu_B g_F B_{\text{ext}} m_F, \tag{2.28}$$

where μ_B is the Bohr magneton and g_F is the Landé g-factor. The linear relation starts to break down, when the hyperfine energy splitting is similar to the energy splitting due to the interaction with the external magnetic field, and the intermediate magnetic field regime is entered. For intermediate fields where the corresponding interaction Hamiltonian neither weakly perturbs nor dominates the hyperfine splitting, the resulting energy splitting will be more difficult to calculate. In general, it requires a diagonalization of the total Hamiltonian numerically, however an exception can be made in the case where $J = 1/2$ or $I = 1/2$. Then the Zeeman energy splitting can be described by [26]

$$\Delta E_{F=I\pm 1/2} = -\frac{h\Delta W}{2(2I+1)} + \mu_N g_I m_F B \pm \frac{h\Delta W}{2}\sqrt{1+\frac{2m_F x}{I+1/2}+x^2}, \tag{2.29}$$

where

$$x \equiv \frac{B(\mu_B g_J - \mu_N g_I)}{h\Delta W}, \tag{2.30}$$

and

$$\Delta W = A\left(I+\frac{1}{2}\right). \tag{2.31}$$

Luckily for us, the atomic species at interest is ^{39}K which has a ground state where $J = 1/2$ and $I = 3/2$ (See figure B.1). What we are interested in investigating is how the ^{39}K $F = 1$ and $F = 2$ hyperfine manifold evolve in the different field regimes which is described by Eq. (2.29) also known as the Breit-Rabi formula. This is shown in figure 2.4 for a uniform magnetic field ranging from 0 to 600 G. Highlighted is the energy states of $F =$

$1, m_F = -1$ and $F = 1, m_F = 0$, since these two states are the ones used in the study of impurity dynamics. Two coils in a Helmholtz configuration, i.e. where the current is running in the same direction in both coils, would produce a uniform field.

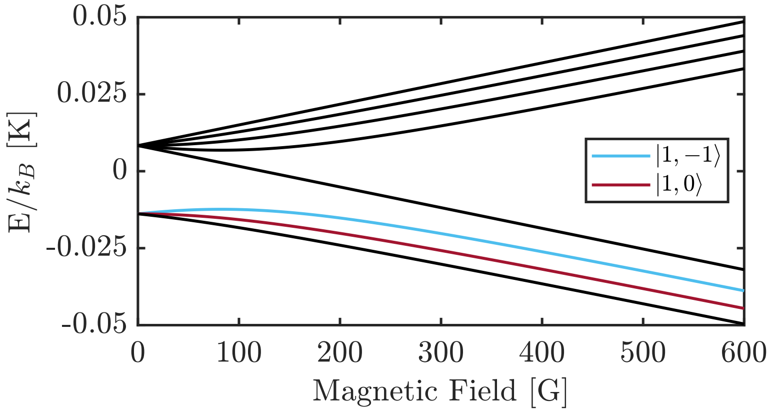

Figure 2.4: Energy levels of ^{39}K atoms in an external magnetic field based on the Breit-Rabi formula (2.29). $F = 1$ is the lower manifold, and $F = 2$ is the upper manifold. In the weak-field regime, i.e. below 50 G the linear behavior can be sensed. The colored states are $m_F = -1$ and $m_F = 0$.

2.4.2 Magnetic compensation gradient

In the previous section, we saw how a uniform bias field lifted the degeneracy of the m_F states in the hyperfine manifold. The goal of this section will be to calculate the necessary magnetic field gradient needed to balance the gravitational potential.

The reason why a magnetic field gradient is needed is because the gravitational potential will be different for atoms in the top of the trap relative to the atoms in the bottom of the trap. One way to produce a

B-field gradient in the laboratory would be to have two coils in an anti-Helmholtz configuration, i.e. two coils shifted vertically and carrying a current in opposite directions, producing a quadrupole field.

Assuming our trap has a height of $D = 30\,\mu\text{m}$, the gravitational potential across the trap can be found by the well-known formula

$$\Delta U_g = m_K g D, \tag{2.32}$$

where m_K is the mass of a single ^{39}K atom and g is the gravitational acceleration. Inserting numbers yields:

$$\Delta U_g = k_B \cdot 1.38\,\mu\text{K}. \tag{2.33}$$

The required energy to balance this gravitational potential must be given by

$$\Delta B \nabla_B E = \Delta U_g, \tag{2.34}$$

where ΔB is the required B-field difference between the top and the bottom of the trap and $\nabla_B E$ is the gradient of the energy states in figure 2.4. The gradient of the energy splitting of $m_F = -1$ and $m_F = 0$ states can be seen in figure 2.5. Finally, we can isolate ΔB in Eq. (2.34) and make a plot of the required B-field needed to compensate for the gravitational potential near the Feshbach resonance located at 526 G. This is shown to the left in figure 2.6. In the right panel in figure 2.6 the magnetic field difference between the top and bottom of the trap is divided by the height of the trap to get the required magnetic field gradient to counteract the gravitational potential. A B-field gradient of about 7.23 G/cm should suffice for the $|1,-1\rangle$ state. The $|1,0\rangle$ state will not be compensated correctly, so atoms in this particular quantum state will tend to drift. The drift can be calculated to see how far the atoms will travel within a typical experimental time. If we say that the experimental time is $t = 10\,\text{ms}$, the atoms in the $|1,0\rangle$-state will approximately drift 1.5 µm which is a fairly small distance given the dimensions of the trap. If we were to pick the other

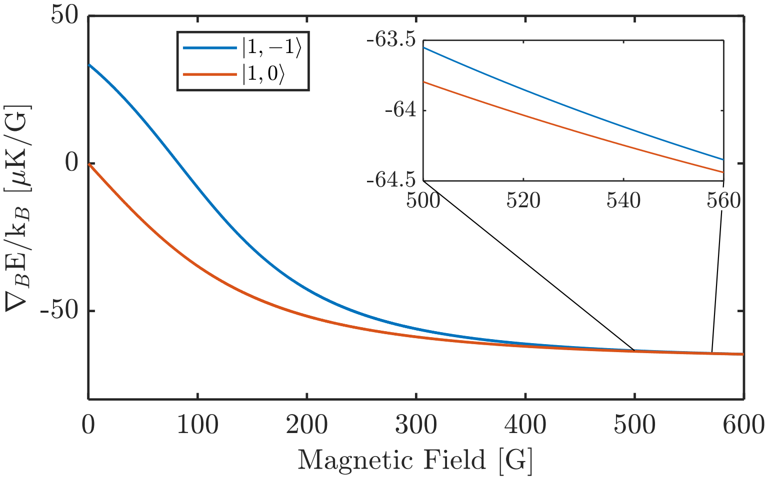

Figure 2.5: Gradient of the $m_F = -1$ and $m_F = 0$ states from figure 2.4. Note that the energy gradient is close to being equal and constant for the two states after 400 G. The inset shows the energy gradient of the two states close to the Feshbach resonance.

Feshbach resonance located at 113.8 G, we could expect a drift of the $|1,0\rangle$ state by more than 1.3 mm within 10 ms of experimental time which would ruin the measurement. Therefore, one should pick a Feshbach resonance close to where the gradient of the energy splitting depicted in figure 2.5 is the same for the two states, which is satisfied at the 526 G resonance.

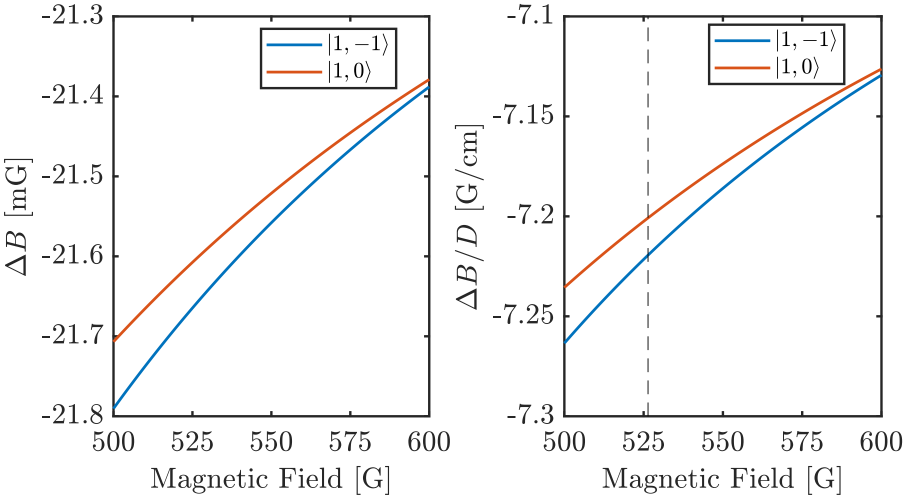

Figure 2.6: Left: Required magnetic field difference between the top and the bottom of the trap, near the Feshbach resonance of the $|1,-1\rangle$ and $|1,0\rangle$ state. Right: Magnetic field difference divided by the height of the trap to get the required magnetic field gradient. The dashed line indicates the center of the Feshbach resonance between the two m_F states.

CHAPTER 3

OPTICAL BOX POTENTIAL

In this chapter, the experimental design of a setup used to generate a hollow cylindrical beam, inspired by the setup in [15], is described. The hollow ring beam will confine the atoms in the radial direction. Unfortunately, time did not allow for the axial confinement to be constructed during this project, and the implementation of sharp end caps will be left as a future prospect.

In the first section, an in-depth look at axicons is given based on calculations done in the ray tracing software: Optics Software for Layout and Optimization (OSLO). This section is needed to understand the behavior of light propagating through an axicon which is an essential piece of equipment in the setup. The full description of the setup is given in Sec. 3.2 together with an analysis of the various distances between each optical element after the fiber. The chapter concludes with a brief description of the evaluation methods in OSLO.

3.1 Understanding Axicons

The first goal in the process of achieving a repulsive hollow cylinder, is to create a beam that expands in a cone-like manner. To alter the geometry of a propagating Gaussian beam coming from an optical fiber, special types of lenses, called axicons or conical prisms [27], can be used. An axicon is rotationally symmetric and has one plano surface and one conical surface. The inclination angle of the conical surface, which we will define as the *axicon angle* θ, does not change with increasing distance from the optical axis. This is different from a regular lens where the angle continuously changes. When the incident light propagates through the conic part of the axicon, the light gets refracted at the glass-air transition (see figure 3.1) and are deviated towards the optical axis. The refracted light then propagates at a *deflection angle* ϕ with respect to the optical axis, which can be derived directly from Snell's law. Under the assumption of a small axicon angle, the deflection angle is approximately given by

$$\phi \approx \theta(n_{glass} - 1),$$

where n_{glass} is the refractive index of the axicon. In the region just after the axicon tip, an interference pattern emerges due to the part of the beam above the optical axis, overlapping with the part of the beam below the optical axis, resulting in a diffraction-free beam. In this region, our beam is propagating as a Bessel beam because the intensity distribution closely resembles that of a Bessel distribution. A true Bessel beam would in principle require an infinite amount of energy to create since each ring generated has the same power. Therefore, this Bessel beam characteristic only applies within the axicon's depth of focus (DOF) [28]. For small axicon angles the DOF can be estimated by

$$DOF \approx \frac{R}{(n_{glass} - 1)\theta},$$

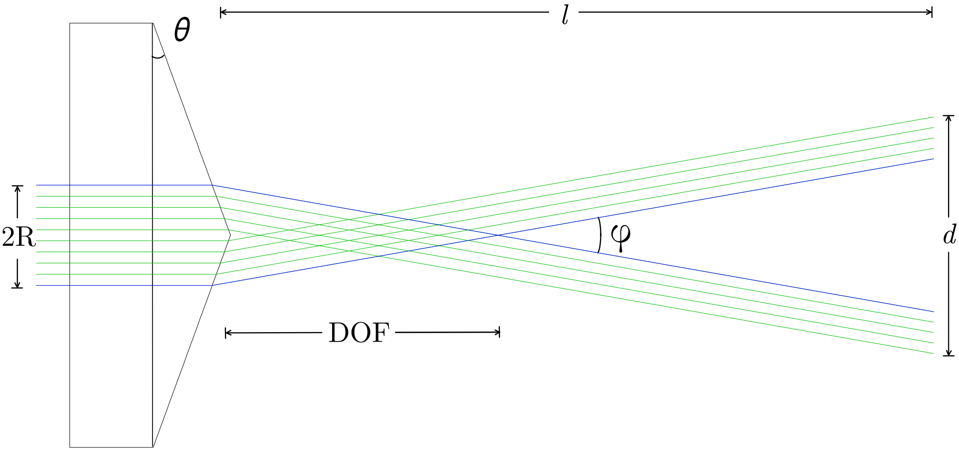

Figure 3.1: Ray tracing simulation for an axicon with an incident beam diameter $2R$ refracted by an axicon angle of $\theta = 20°$. Blue rays start on the outside of the incident beam and end up on the inside after the Bessel region.

where R is the radius of the incoming beam. From this simple expression it is clear, that when the axicon angle gets smaller, the DOF, i.e. the extent of the Bessel region, increases. In the far-field, i.e. after the Bessel region, the deviated beams ceases to overlap, and the intensity becomes distributed on a ring with a thickness closely related to the incident beam radius R. At last, the diameter, d, of the ring can be found by a simple trigonometric calculation where the expression for the divergence angle ϕ was inserted

$$d = 2l\tan\phi = 2l\tan(\theta(n_{glass} - 1)),$$

where l is the length shown in figure 3.1. This equation is only valid as long as $l \gg DOF$ and $d \gg R$.

The behavior of light passing through a single axicon is now known. The first problem to arise is of course that the beam expands in a cone-like shape. For a repulsive optical trap to work in practice, some degree of collimation is required. The easiest way to achieve a non-divergent collimated ring is to introduce a second axicon. This can be seen in figure 3.2. It is important, that the axicon angle of both axicons are the same.

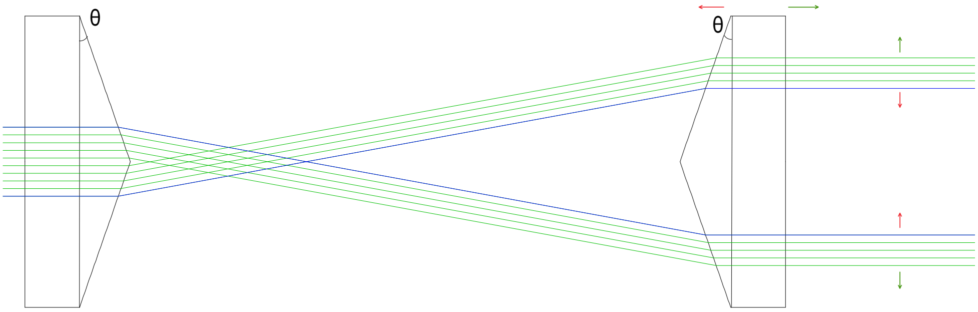

Figure 3.2: Ray tracing simulation of a system of two axicons with the same axicon angle. The first axicon splits the incident beam into a diverging ring. The second axicon collimates the geometry of the beam and a cylinder with a constant radius is achieved. By moving the second axicon to the left (designated by the red arrow above it) will result in a smaller ring beam diameter. Likewise, if the second axicon is moved to the right (designated by the green arrow), the ring beam diameter is increased.

Small deviations will lead to either a divergent- or convergent beam. In addition, the two axicons must have their tips facing each other to achieve collimation. From the ray tracing sketch in figure 3.2, it can be seen that the diameter of the collimated ring is governed by the mutual separation of the axicons. By moving the second axicon to the left will result in a smaller ring and vice versa.

So far, the geometry of the setup was the main focus and this has yielded a collimated ring with a hollow center (at least according to the ray tracing simulation). It is now time to discuss the intensity distribution of the ring. When we approach the annulus going from the center of the ring, we would not expect to see a sharp increase in intensity, due to the fact that a Gaussian beam is the propagating beam through the first axicon. A Gaussian beam with the fundamental transverse electromagnetic mode (TEM_{00}), is characterized by having the highest intensity in the center compared to the wings of the beam. It is clear from the ray tracing figures 3.1 and 3.2, that the rays closest to the optical axis (the most intense light for a Gaussian beam) will get refracted in a way such that they end up on the outside of the beam after the Bessel region. Meanwhile, the two outermost rays (less intense for a Gaussian beam), which are blue colored, are now on the inside. This of course leads to a graduate increase in intensity until we reach the outer region of the annulus where it suddenly drops fast. In this paper [29] they make a theoretical model of the transverse intensity amplitude in the far-field region of the first axicon and compare it with an experimental intensity profile. Here they demonstrate the influence of an imperfect apex tip of the axicon. They show, by introducing a bluntness to the axicon tip in the theoretical model, that they can achieve an almost perfect agreement between theory and experiment. The tail of residual light does not gradually decrease towards the center but is rather expressed in form of inner contrasted secondary rings due to diffraction of the imperfect axicon tip. These inner rings are not optimal when designing a hollow repulsive optical trap. A natural way to circumvent this problem, is to place an opaque mask that blocks all the secondary rings which have been demonstrated both in [29] and [14]. The price you pay for going with this kind of setup is, that you cannot be able to change the size of the ring without changing the aperture size of your mask.

A setup that could somehow invert the ring such that the residual light is on the outside of the main ring, instead of on the inside, would be preferable. One would still have the opportunity to change the diameter of the ring without being concerned about a matching mask. This was exactly done by a group in Hamburg [15], where a detailed description of their setup can be found in [30]. A setup of this kind will require not only three axicons, but also two lenses that all together will invert the ring and produce steep inner walls at an intermediate image plane, determined by the foci of the lenses. When you combine axicons and lenses, it starts to get a bit more complicated. Although axicons are not supposed to shift the point of focus, there will always be a small separation between the focus point of the lens and the actual focus of the ring. This has been reported in [29] and can also be observed in OSLO by comparing the paraxial focus with and without axicons inserted. A full description of the setup will be presented in the next section based on ray tracing simulations from OSLO.

3.2 Three Axicon setup

The first step would be to simulate the out-put light coming from the optical fiber being used, which is highly divergent. The single-mode fiber used in the lab has an operating wavelength from 400 to 680 nm, thus compatible with the laser pointer being used, which is capable of producing up to 60 mW of 532 nm light. What characterizes the beam expansion is the numerical aperture of the fiber. The numerical aperture (NA) of a fiber is defined as the sine of the largest angle an incident ray can have for total internal reflectance to occur in the core [31]. For a single-mode fiber, it is relatively straightforward to determine a fiber's NA. This is done simply by measuring the divergence angle of the light cone it emits. To obtain the divergence angle, a measurement of the beam-width as a function of z-distance, which is the distance along the optical axis, must be made. The CMOS camera used is mounted on a translational stage, controlled by a micrometer screw where the z-distance can be accurately read. The characteristic beam-width ($1/e^2$) was obtained using a Gaussian fitting tool in a LABView program. The x and y diameters of the beam can be seen in figure 3.3. We can obtain the slopes from the fits, and then simply use trigonometry to get a value for the NA of the fiber. For the x-direction, the calculated NA will be $\mathrm{NA}_x = 0.0556$, and

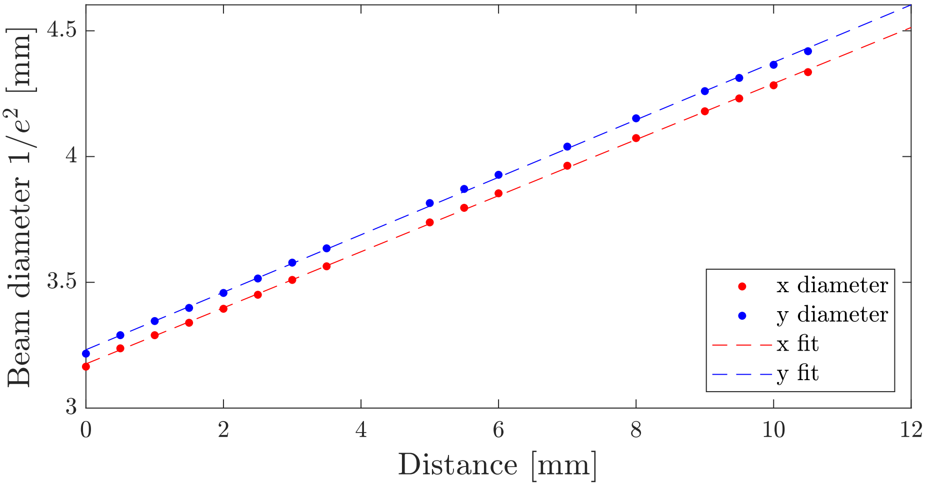

Figure 3.3: The beam diameter of light coming out of an optical fiber as a function of z-distance for both the x- and y direction together with linear fits. The zero point on the x-axis is just a reference point, and not the actual distance from the fiber tip.

for the y-direction, the calculated NA is $\mathrm{NA}_y = 0.0570$. Taking the mean of these two numbers gives NA= 0.0563. This value can then be passed on to OSLO, as our object's numerical aperture. In principle, the optical fiber tip can be seen as an object, that we want to transform into a hollow cylinder. Next up is the out-coupler lens, whose task is to collimate or focus the light coming out of the fiber. The lens used is an aspheric lens from Thorlabs with a focal length of $f = 4.60\,\mathrm{mm}$. Aspheric lenses can be characterized by several parameters and have a surface profile given by the aspheric lens design formula [32]:

$$z = \frac{Cr^2}{1+\sqrt{1-C^2(1+k)r^2}} + A_0 + A_1 r + A_2 r^2 + A_3 r^3 + A_4 r^4 + \ldots \tag{3.1}$$

Here z is the surface sag, C is the curvature, r is the radial coordinate, k the conic constant and A_i the coefficients of a correction polynomial that allows for a higher-order aspheric optical element to be defined. Where a regular spherical lens can be described by two surfaces, each with its own curvature and of course the refractive index, an aspheric lens can be more complex and involve several aspheric coefficients. Luckily, this information can typically be gathered from the manufacture.

The out-coupler lens and the fiber are put in a cage system configuration, where the distance between the fiber tip and out-coupler lens can be varied by a z-axis translation mount with micrometer precision. This degree of freedom turns out to be crucial in the pursue of a sharp thin inner ring. Increasing the distance between the fiber tip and out-coupler lens leads to a divergent beam, whereas a decrease leads to a convergent beam. The next optical element in the line is the first axicon which we know from Sec. 3.1, transforms a Gaussian beam into a Bessel beam in the near-field, and in the far-field a divergent ring takes shape. The axicons in OSLO can be modelled by treating them as aspheric lenses where only the linear coefficient in Eq. (3.1) is included. The relation between the axicon angle and the coefficient A_1 is simply given by $\tan\theta = A_1$ [33]. At this point, the residual light is present inside the ring. To make the optical inversion of the ring, a combination of two optical elements, an achromatic doublet lens and an axicon, are needed. The achromatic lens focuses the ring while keeping the effects of spherical and chromatic aberration at a minimum. The second axicon, which is placed just after the achromat, inverts the ring and ensures that no residual light remains on the inside of the ring. After the point of optical inversion, the residual light resides on the outside of the inner ring. Finally, the now divergent ring can be collimated, by inserting a third axicon with the correct axicon angle, which of course must be placed after the point of optical inversion. Depending on the aspheric out-coupler and achromatic lenses, and their mutual distance from each other, an intermediate image plane forms. The intermediate image plane is the plane in space, at which the ring is sharpest and has the thinnest inner ring. Ideally, this is located somewhere after the third axicon. A full sketch of how the setup appears on the optical breadboard in the laboratory, can be seen in figure 3.4.

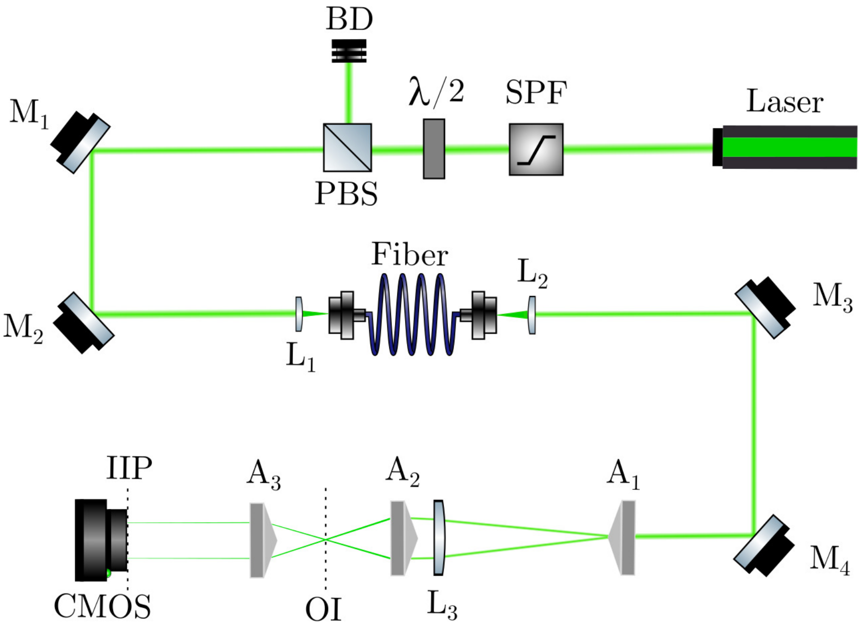

Figure 3.4: Full sketch of the setup until arriving at the intermediate image plane (IIP). A beam of 532 nm light goes through a short-pass filter where light with a wavelength of 550 nm or higher gets reflected. A combination of a $\lambda/2$ waveplate and a Polarizing Beamsplitting cube (PBS) makes it possible to adjust the transmitted intensity through the cube. What is not transmitted gets directed into a beam dump (BD). After two mirrors, the beam arrives at an in-coupler lens (L_1) that focuses the beam into the optical fiber, where it meets an out-coupler lens (L_2) at the exit. The beam then gets reflected by two mirrors again and arrives at the first axicon (A_1). The axicon, A_1, splits the beam into a ring beam where the combination of an achromatic lens (L_3) and a second axicon (A_2) causes the optical inversion (OI). Finally, the third axicon (A_3) collimates the geometry of the ring, and a camera with a CMOS image sensor chip is placed at the IIP for image capturing.

Two setups with different achromatic lenses, i.e. different focal lengths and axicon angles, have been studied both in the laboratory and in OSLO. A table that shows the optical components in each setup is shown in table 3.1. The 200 mm setup is self-designed, and the 400 mm is similar to that used in [15] but with another out-coupler lens.

	A_1 [degree]	L_3 [mm]	A_2 [degree]	A_3 [degree]
200 mm setup	5	200	10	10
400 mm setup	10	400	10	2

Table 3.1: Optical components used in the two configurations which I have titled the 200 mm and 400 mm setup.

In the next section, I will discuss what will happen when distances between each optical element after the fiber are varied based on the corresponding OSLO simulations for each of the two setups in table 3.1. I will refer to the abbreviations of each optical element as they appear in figure 3.4.

3.2.1 Distance analysis

As mentioned earlier, the distance between the fiber tip and L_2, which I will call S_1 from now on, seems to play a crucial role in where the position of the IIP is located. By tuning S_1, one can arbitrarily choose where the focus of the ring will be. If the ring diameter of both setups is kept the same, and S_1 is set such that the initial position of the IIP is right after A_3 in both setups, the influence of a varying S_1 on the focus shift can be studied in OSLO. This variation is exactly shown in figure 3.5. If we increase the variation distance to 0.1 mm the 200 mm setup leads to a focus change of 165 mm whereas for the 400 mm, it goes to infinity for the same variation. The 400 mm setup in particular, seems to be very sensitive to this variation, at least when combined with the chosen L_2. In addition

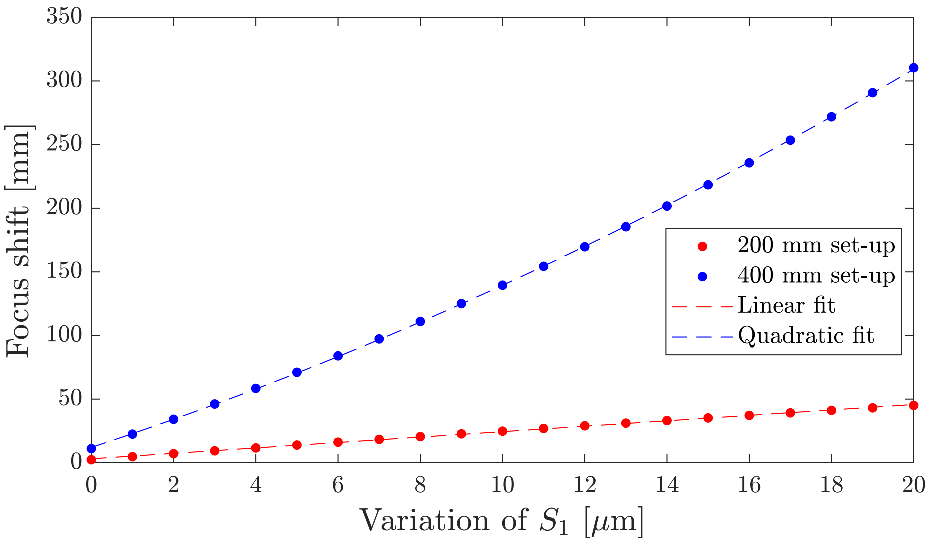

Figure 3.5: Focus shift as a function of out-coupler lens distance obtained from ray tracing simulations in OSLO. The starting point of S_1 was set such that both setups have the IIP right after A_3. For the 200 mm setup the starting point of $S_1 = 2.7546$ mm and for the 400 mm setup $S_1 = 2.711$ mm. The matching fits for both setups are also different. For the 200 mm a linear fit is perfect, and for the 400 mm a quadratic fit is made.

to the focus shift, S_1 also has an impact on the amount of diffraction that are present in the system. Then there is the distance between L_2 and A_1, which I will refer to as S_2. For the 200 mm setup S_2 was varied 300 mm, and resulted in a focus shift of only 3 mm. For the 400 mm setup, a variation of 300 mm yielded a focus shift of 73 mm, which is still nothing compared to what we saw with S_1. Having this wiggle room is great for practical purposes, when constructing the setup in the laboratory knowing that S_2 is of minor importance. The next distance is between A_1 and L_3, called S_3. Obviously, S_3 has an impact on the geometry of the system. It does not change the location of the IIP, but it affects the size of the ring at the IIP. What is interesting is that the collimation of the ring beam after A_3 is highly dependent on S_3. There is a sweet spot for S_3 for both setups, at which the ring remains collimated. For the 200 mm setup, $S_3 = 208(2)$ mm equivalent to a ring diameter of 16.55 mm at the position of L_3. For the 400 mm setup, $S_3 = 81(2)$ mm equivalent to a ring diameter of 12.9 mm at L_3. Increasing S_3 beyond this sweet spot leads to a divergent ring beam at the IIP and vice versa. The next distance, which is the one between L_3 and A_2, is of minor concern. The only thing that happens, is that you push the point of optical inversion by the same amount you change the distance in the first place. It does not really affect the collimation nor the location of the IIP. For that reason, A_2 is placed as close to L_3 as practically possible. Since the optical elements are in a cage system configuration in the laboratory, the distance can be reduced to less than one centimeter. The distance between A_2 and A_3 determines the size of the ring. Obviously A_3 must be placed after the point of optical inversion in order to achieve sharp edges on the inside of the ring. Finally, the distance between A_3 and the CMOS camera, can be found using the paraxial focussing method which will be described in section 3.3.3. A full spreadsheet containing information about the surface curvature radius, separation, aperture radius and glass material for each optical element for the 200 mm and 400 mm setup, can be found in appendix A.

3.3 Ray tracing simulations

To get a better understanding of how the propagation of light responds, when different optical elements are inserted in the beam path, a ray tracing software like OSLO is highly valuable. The whole optical system can be simulated and drawn simply by providing the radius of curvature, thickness and refractive index of each surface in your system. The setup can then be displayed in a 2D or 3D drawing where ray-tracing algorithms will show the optical path of light rays through the system. This could of course be done by hand using a ray transfer matrix analysis, however using computers to do this for us will save a lot of time. Some of the key features that will be used in OSLO, are the paraxial focussing method and spot diagrams described in two separate subsections, but first I will present descriptions of the two image evaluation methods that OSLO provides.

3.3.1 Geometrical evaluation

Solving physics problems often involve approximations and optics is no exception. The main simplification in geometrical optics, is that we can describe light propagation in terms of rays obeying Fermat's principle, and thereby completely ignore the wave nature of light. Optical effects such as interference and diffraction will be neglected under the geometrical approximation analysis, however for imaging and the study of aberrations effects, the ray tracing tool is excellent. Diffraction becomes less significant in the conceptual limit as the wavelength gets much smaller than the physical dimension of the optical system, and an idealized domain of geometrical optics is achieved [34].

3.3.2 Diffraction evaluation

For wave-like phenomena to be included, like diffraction and interference, some kind of wave equation needs to be solved. In general, one would try to solve Maxwell's equations, however for most optical design problems, one can reduce the problem to a scalar wave problem instead of a vector wave problem [35]. This corresponds to looking for a solution to the Helmholtz equation given by

$$\nabla^2 f(x,y,z) = -k^2 f(x,y,z). \tag{3.2}$$

The scalar field $f(x, y, z)$ is approximated by OSLO to be a field described by a geometrical wavefront, which is a wavefront constructed according to the laws of geometrical optics. By this construction, a diffraction analysis can be performed to e.g. give the diffraction-limit of the optical system. In a geometrical analysis with no aberration, the rays emanating from an object point going through a lens would converge at a single image point, but what wave theory predicts is that the image will be of a finite size, which is called the diffraction limit. Therefore, the resolution of your image can either be limited by aberration or diffraction effects.

3.3.3 Focussing method

In order to find the image plane at which our image of the object is in focus, a focussing method in OSLO is used. By solving for an axial ray height equal to zero for the last surface before the image surface, will yield the paraxial focus distance of the selected surface thickness [36]. The paraxial focus coincides with the plane at which the ring width is smallest. This can be used to quickly identify where one would expect the image plane to be in the laboratory.

3.3.4 Spot diagram

An especially useful feature in OSLO is the spot diagram. The spot diagram shows a map of the pattern of rays incident on the image surface. In this plot, one can get a good idea of how the image of the object will look, and easily see how the image changes before and after the focus plane. It is particularly useful for this project since it also provides the radius of the object (which in this project is a ring). Furthermore, the field points created for each traced ray can be easily imported to other analysis tools such as MATLAB for further investigations. This is exactly done in figure 3.6, where the spot diagrams of the 200 mm and 400 mm setup are shown. These spot diagrams are evaluated at the paraxial focus that was just described in the previous subsection. In the spot diagrams, an estimate of the diffraction limit is given as the radius of an airy disk. The airy disk, which is imposed by diffraction, is the smallest point to which a beam of light can be focused. A qualitative comparison can then be made of the geometric image (spot diagram) to the limiting spot size (airy disk).

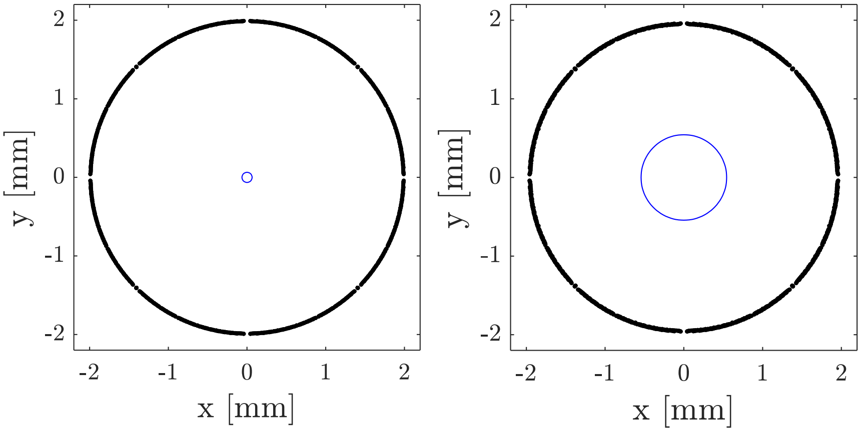

Figure 3.6: Spot diagrams imported from OSLO with 1996 traced rays evaluated at the paraxial focus. The left figure shows the spot diagram for the 200 mm setup, and the right figure shows the spot diagram for the 400 mm setup. From these diagrams, the width and the diameter of the ring can easily be extracted. It is important to stress, that the spot diagrams do not indicate the irradiance in the image as the plot does not show any weighting of the rays. The blue circle at the center of each plot shows the corresponding airy disk.

It is clear from figure 3.6 that the diffraction limit is significantly different for the two setups, in fact they differ with almost one magnitude. This serves as an early indication of what performance we can expect from the two setups, with the 200 mm being superior to the 400 mm setup.

CHAPTER 4

CYLINDRICAL BOX CHARACTERIZATION

In the following chapter, I present the characteristics of the repulsive hollow cylinder generated by the setup described in the previous chapter. This includes both results for the 200 mm and 400 mm setup. Although, it was quickly realized that the 400 mm setup did not yield what was expected, it is still included. The chapter has two main sections; Sec. 4.1 is related to the ring characteristics at the intermediate image plane, while Sec. 4.2 is concerned with the ring at the image plane. The 8-bit images which are used to evaluate the properties of the ring are taken by an IDS camera [37]. It has a CMOS sensor type with a Quantum Efficiency of about 60% in the green light region of the visual spectrum. The resolution of the camera (horizontal × vertical) is 1280 × 1024 pixels with a pixel size of 5.3 µm × 5.3 µm yielding a chip size of 6.784 mm × 5.427 mm where the exposure time can be varied between 0.009 ms-2000 ms.

4.1 Box characteristics near the intermediate image plane

In this section, the various characteristics of the ring potential are presented. This is done at the intermediate image plane, easily accessible for evaluation.

4.1.1 Wall steepness

Ideally, a box potential of a depth U_0, containing atoms with a kinetic energy of $k_B T$ with $U_0 \gg k_B T$, would confine the atoms in a way that yields a perfect uniform and homogeneous distribution. The perfect box potential is characterized by having infinite steep walls, however this is not realizable in practice, so the potential will rise at a finite rate as shown in the following. The wall steepness is characterized for both the 400 mm and the 200 mm setup starting with the former.

400 mm setup

The first setup to be presented is the one with the 400 mm achromatic lens inserted. The raw 8-bit image of the ring taken at the intermediate image plane (IIP) can be seen on the left panel of figure 4.1. One pixel can yield values between 0 and 255 depending on the received light intensity, where 0 corresponds to the black color and 255 corresponds to white at which saturation is achieved. The light intensity distribution can be better visualized in the right panel. Here a color bar with the corresponding pixel values is included. It can be seen that the color bar only extends to a pixel value of 150, meaning that the picture taken is far from saturation. The first thing to notice is that the residual light, i.e.

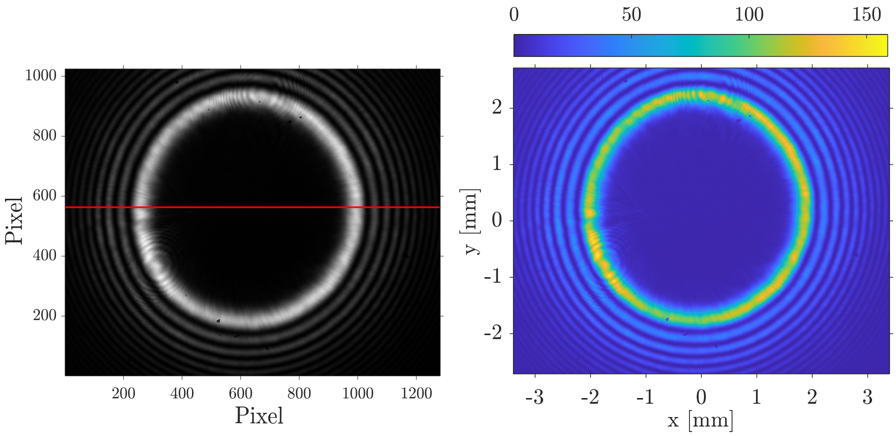

Figure 4.1: Left: Raw grayscale image of the 400 mm setup at the IIP, with pixel number on both axes. The red line is the cut shown in figure 4.2. Right: Corresponding color image with axes converted to real length scales and a color bar of pixel values included to distinguish intensity differences.

the secondary rings, are on the outside of the intense inner ring. This confirms that the optical inversion has taken place. To check whether this ring has “box-like” characteristics, an intensity profile of a cut through the ring can be evaluated. The cut is shown as the red line in figure 4.1, and the intensity distribution of this cut is shown in figure 4.2. The cut shows that the ring is close to being hollow, with almost zero residual intensity in between the two inner peaks in figure 4.2. It was mentioned earlier that the additional rings generated by the axicons can be attributed to the imperfections in the tips of the axicons leading to diffraction. This is however not of great concern as long as they are not present inside the intense inner ring. The only downside is a loss in power, which can be circumvented by having a powerful enough laser. To evaluate the steepness of the wall, a power law of the form $I(x) = bx^a$ is fitted to one

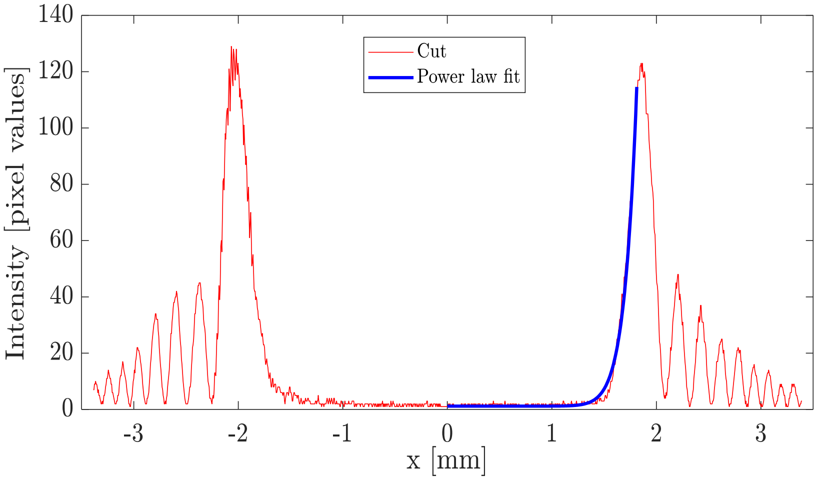

Figure 4.2: An intensity profile of a cut through the ring of the 400 mm setup corresponding to the red line segment in figure 4.1. The vertical axis shows the intensity expressed in pixel values. A power law on the form $I(x) = bx^a$ is fitted to one half of the inner ring depicted as the blue curve.

half of the cut, shown as the blue curve in figure 4.2. The parameters b and a are used as fitting parameters where in particular a is of great interest. The resulting fit yields $a = 14.91(32)$ just in between what is achieved in [13] ($a = 13(2)$) and [14] ($a = 16.2(16)$).

Besides the steep inner walls of the ring, it is also critical to have a uniform intensity distribution around the ring. Therefore, it is important to investigate other segments of the ring. One can make a simple rotation around the origin by multiplying the line with a 2D rotation matrix. The governing angle θ of the rotation matrix can then range from 0° to 180°. The resulting peak intensity variation around the inner ring can be seen in figure 4.3. Ideally, the curves in figure 4.3 should be constant, but this is not realistic in practice. As long as the intensity variations around the

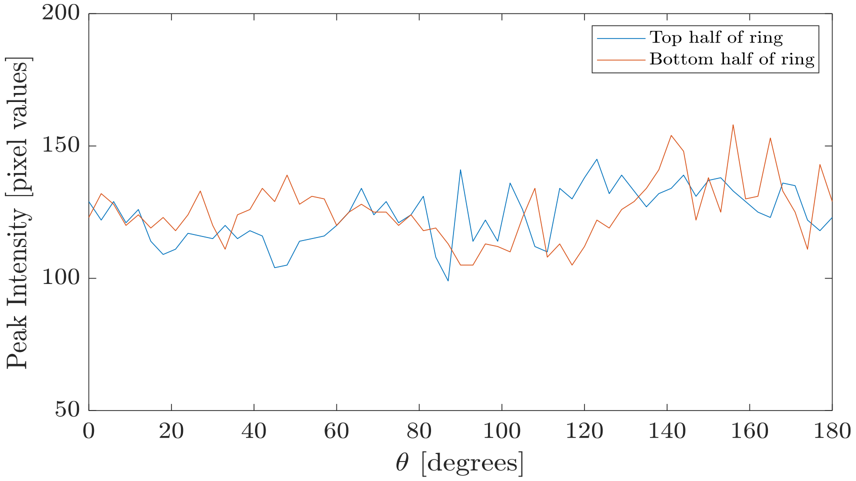

Figure 4.3: Peak intensity as a function of angle around the ring (rotation direction is anti-clockwise) for the 400 mm setup. The red horizontal line in figure 4.1 corresponds to $\theta = 0°$. The blue curve shows the peak intensity of the upper part of the ring, while the orange curve shows the bottom half. Each data point is taken with an increment of 3°.

ring are much smaller than the actual peak intensity, the atoms should not feel any difference.

Now that the peak intensities around the ring have been obtained and their corresponding x-values, a precise estimate of the diameter of the ring can be calculated. This is done by taking the point of the peak intensities for each line segment and calculate their difference. The diameter of the ring in figure 4.1 is calculated to be $d_{\text{ring}} = 3.944(13)\,\text{mm}$.

Finally, the width of the ring was determined by taking the full width at half maximum (FWHM) for each peak intensity around the ring. This yielded a width of $w_{\text{ring}} = 238.3(90)\,\mu\text{m}$.

200 mm setup

We saw with the 400 mm setup that it yielded a scaling of $I(x) \propto x^{14.91(32)}$. This is still far away from what was achieved in [15] ($a = 87(4)$) even though many of the optical components were the same, except for the out-coupler lens L_2. Another setup was tested in the laboratory, where the 400 mm lens was substituted with a 200 mm achromatic lens instead. The reasoning for testing this new setup, was because it showed promising results in OSLO: the sharpness of the ring, the low diffraction limit and the reduced space it required on the optical breadboard. A captured image at the IIP can be seen in figure 4.4. Clear differences can be seen when comparing this figure with figure 4.1. It appears that more of the intensity is in the inner ring, and the diffraction pattern that was visible in the 400 mm setup is no longer directly observable. The raw image

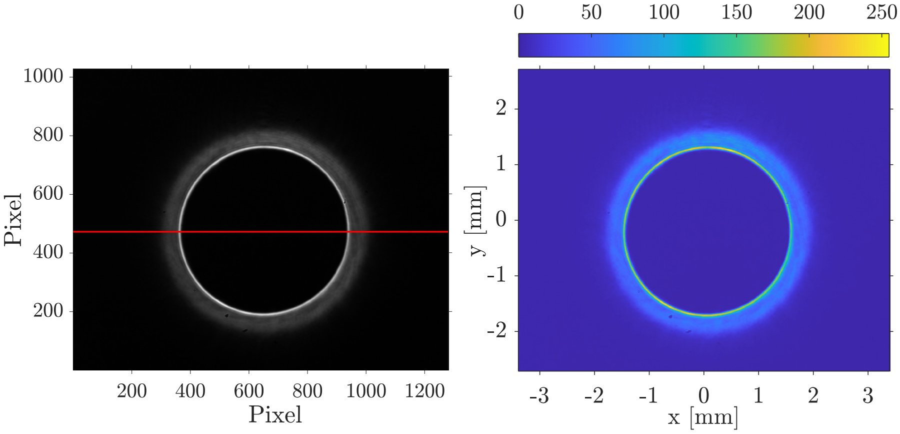

Figure 4.4: Left: Raw grayscale image of the 200 mm setup at the IIP, with pixel number on both axes. The red line corresponds to a cut evaluated in figure 4.5. Right: Corresponding color image with axes converted to real length scales and a color bar of pixel values included to distinguish intensity differences.

of the ring shows a hard cut-off between the inner ring and the hollow center. The intensity profile of the indicated red line in figure 4.4 can be seen in figure 4.5. The obtained power law fit for the 200 mm setup

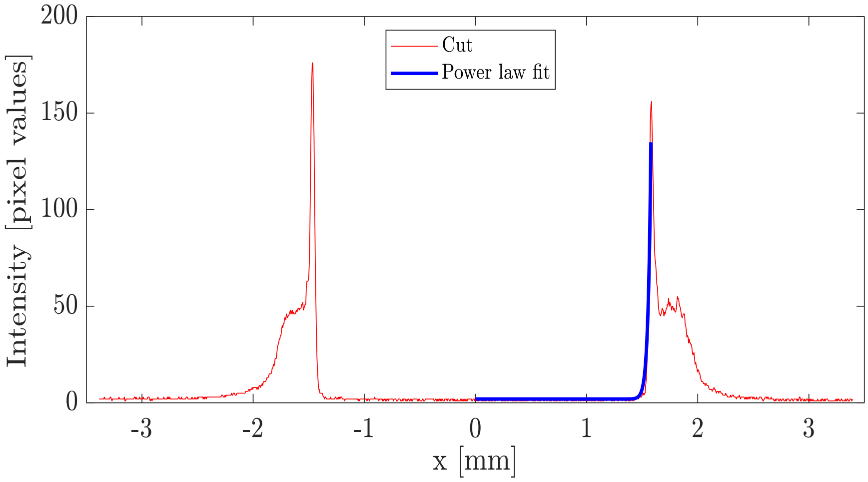

Figure 4.5: Intensity profile of a cut through the ring of the 200 mm setup corresponding to the red line in figure 4.4. The vertical axis shows the intensity expressed in pixel values. A power law on the form $I(x) = bx^a$ is fitted to one half of the inner ring depicted as the blue curve.

resulted in a scaling of $I(x) \propto x^{60.3(34)}$ which is significantly higher than the one achieved with the 400 mm setup. Now that the intensity profile for a single line segment is found, the intensity profile for the rest of the ring can be evaluated following the same procedure used for the 400 mm setup. The different peak intensity values around the ring, can be seen in figure 4.6. The diameter of the ring at the IIP is estimated to be $d_{\text{ring}} = 3.033(4)$ mm and the measured width around the ring is $w_{\text{ring}} = 51.3(19)\,\mu$m. The highest intensity variations around the ring are on the order of 100 pixel values, whereas for the 400 mm setup this number was closer to 50. The high intensity variations around the ring for

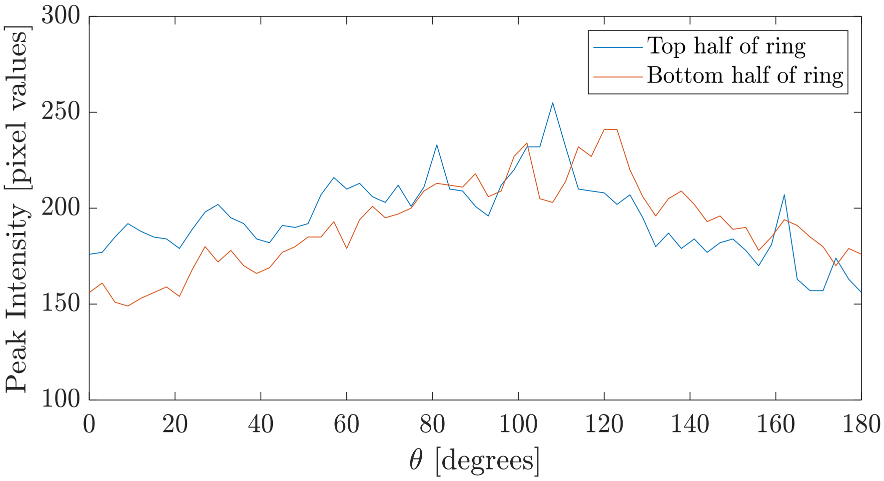

Figure 4.6: Peak intensity as a function of angle around the ring (rotation direction is anti-clockwise) for the 200 mm setup. The red horizontal line in figure 4.4 corresponds to $\theta = 0°$. The blue curve shows the peak intensity of the upper part of the ring, while the orange curve shows the bottom half. Each data point is taken with an increment of 3°.

the 200 mm setup can be caused by small miss alignments in the beam path through the optical components. It is important to stress, that we are approaching a resolution problem of the camera when evaluating the width of the ring for the 200 mm setup. In fact since we have a pixel size of 5.3 µm and the obtained width of the ring was $w_{\text{ring}} = 51.3(19)\,\mu\text{m}$, we only have around 10 pixels on average to resolve the width.

4.1.2 Third axicon position variation

To have the degree of freedom to easily change the diameter of the ring is a unique feature of this setup. It is therefore an interesting property to study. One way to characterize it, is to see how the diameter of the ring changes when the distance between A_2 and A_3 in figure 3.4 is varied. This is shown for both the 200 mm- and 400 mm setup in figure 4.7. In this figure, the data obtained in the laboratory is also compared to corresponding OSLO simulations of the diameter at different A_3 positions. The camera had been placed at the IIP, however for the 400 mm setup it was difficult to say whether the camera was exactly placed in the focus plane or not. What one can do to make sure that the camera is placed at the IIP is to check the width of the ring at various points along the optical axis, this is further studied in the next section. Regardless of the issue related to the image-plane determination of the 400 mm setup, figure 4.7 shows a linear relation between the diameter of the ring, and the position of the third axicon along the z-direction. This is further supported by

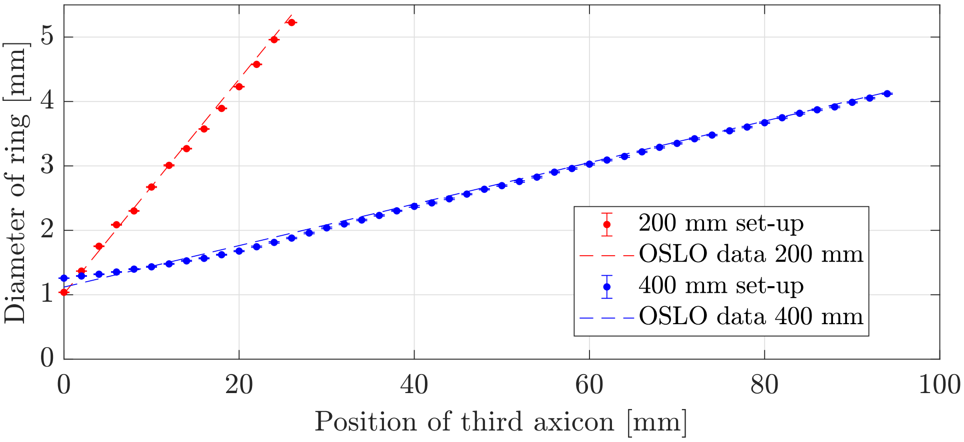

Figure 4.7: Diameter of the ring at the IIP as a function of the position of A_3 for the 200 mm (red)- and 400 mm (blue) setup. The measurements done in the laboratory show a clear linear relation between the diameter of the ring and the position of the third axicon. This is also verified by the simulations done in OSLO shown as the dashed lines.

the corresponding OSLO simulation which predicts the same behavior. Linear fits were made to both data sets (fit not shown in figure 4.7), which yielded a slope of 0.160(2) for the 200 mm setup, and thus for each mm A_3 is moved away from A_2, the diameter of the ring at the IIP changes by 160(2) µm. For the 400 mm setup the fit yielded a slope of 0.0319(4) equivalent to a diameter change of 31.9(4) µm per mm A_3 is moved away from A_2. The upper limit on the ring diameter, at which the data in figure 4.7 was gathered, is of course set by the dimensions of the camera chip. The lower limit is set by the point of optical inversion. Approaching the point of optical inversion with A_3, will result in a distorted ring, which is highly susceptible to small misalignments in the setup. Therefore, a lower limit of at least 1 mm for the ring diameter at the IIP for both setups should be maintained.

4.1.3 Wall width

Another important characteristic of the setup to investigate, is how the width of the inner ring changes along the z-direction. In the effective focus of the two lenses used in the setup, i.e. at the IIP, the inner ring has a higher peak intensity, and thus a thinner ring width compared to a ring away from the IIP. The position of the IIP can be found by plotting the width as a function of distance along the optical axis. This is done for the 200 mm setup in figure 4.8. The width of the ring in OSLO, is obtained through the spot diagram analysis. Specifically, the widths were extracted by taking the norm of a ray located on the outer rim of the ring minus the corresponding ray from the inner rim. One data point in the laboratory in figure 4.8 is obtained, by taking the mean value of the FWHM of each peak intensity around the ring. The same procedure is performed for all the other 206 data points that are presented in the figure. The reason why there exist gaps in between every 36 data point is because the distance between two mounting holes on the optical breadboard is 25 mm, and the translational stage where the camera is mounted on top only covers

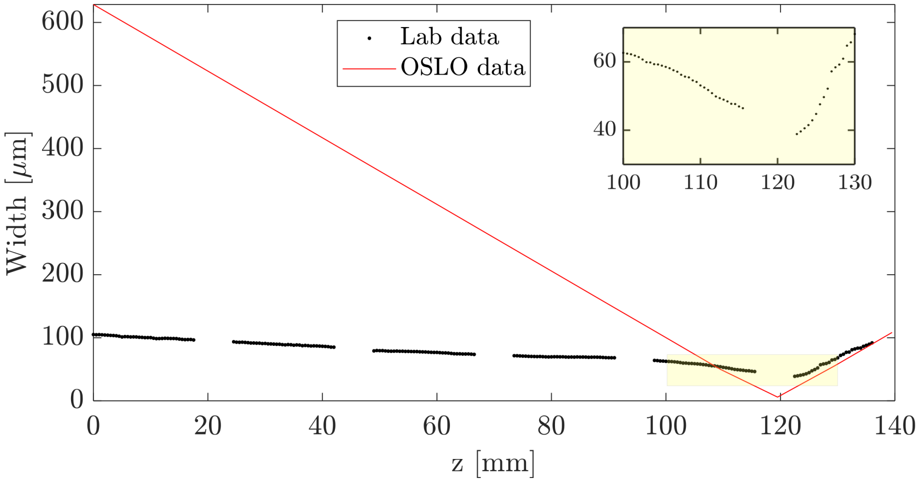

Figure 4.8: Width of the ring as a function of z-distance for the 200 mm setup, together with a simulation prediction in OSLO. Both data sets seem to agree that there exists a linear relation between the width of the ring and the z-distance before and after the IIP. The inset shows the width of the ring obtained in the laboratory in the vicinity of the focus plane, i.e. the IIP. The faint yellow rectangle depicts the area which the inset covers.

18 mm per mounting hole, leaving out a gap of 7 mm at each sequence. First to note in figure 4.8, is the extremely high discrepancy between data obtained in the laboratory and the prediction from OSLO. From the reference point at $z = 0$ mm, to the minimum at which the IIP is located, there is little to no agreement. First after the minimum, the two data sets seem to agree on the width of the ring. The discrepancy can perhaps be explained by the following: First, the diffraction pattern in the shape of secondary rings, are only visible right up to the point where we have the IIP located. At the IIP and beyond, i.e. the last data points in figure 4.8, the diffraction pattern ceases to exist, and we are left with a faint blurry outer ring shown in figure 4.4. Now, since this diffraction phenomenon

does not appear on the spot diagram in OSLO at all due to the nature of geometrical optics, the way of determining the width of the ring from the spot diagram, might not be comparable with the data obtained in the laboratory. However, it is remarkable that the two data sets tend to agree after the IIP, where no clear diffraction pattern exists. Another thing to note is the width, predicted by OSLO at the IIP, which is on the order of a few µm. This is highly idealized and cannot really be compared to what is seen in the laboratory. To make a real comparison between the laboratory data and the width predicted by OSLO, one would need to include the corresponding resolution limit and not just rely on the geometrical optics prediction.

By using the same images taken to produce what is seen in figure 4.8, the diameter of the ring can be extracted as well, to study how it changes as a function of z-distance for the 200 mm setup. The result can be seen in figure 4.9. It appears that the diameter of the ring is not constant over a distance of 140 mm. This means, that the ring beam cannot be considered fully collimated. It was mentioned in the previous chapter in Sec. 3.2.1, that the distance between the first axicon and the achromatic lens (S_3) had an influence on the collimation of the ring beam. This poses the question of whether the correct distance was used in the laboratory. Since we have what appears to be a converging ring beam, an increase of the distance S_3 could possibly give a less converging ring beam.

4.2 Box potential at the image plane

So far, the generated repulsive hollow beam was characterized at the IIP, where the diameter of the ring is on the order of millimeters. Such a trap is far too large to capture the amount of potassium atoms that are present in a typical experiment in the MIX laboratory. In [11] the size of the BEC is on the order of 50 – 65 µm after a time of flight period of 18 ms depending on the desired scattering length, thus a trap dimension

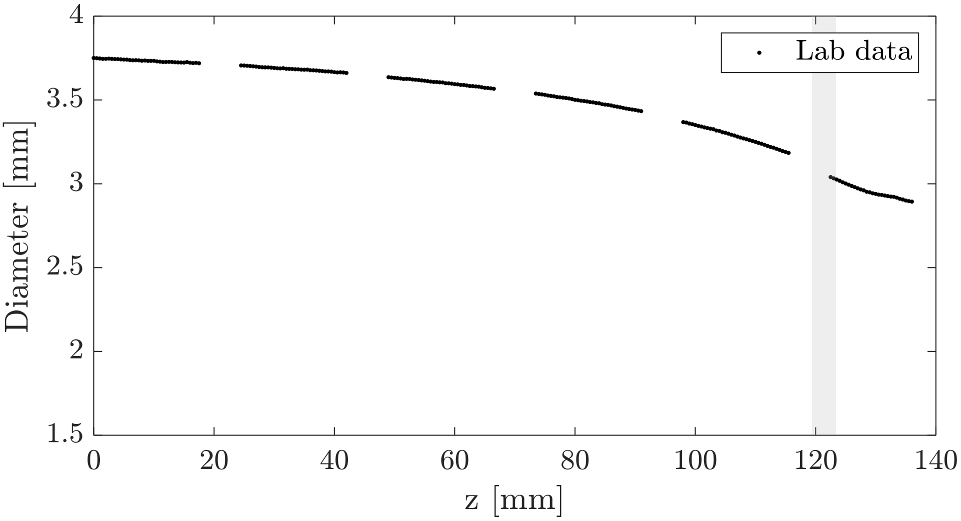

Figure 4.9: Diameter of the ring as a function of z-distance for the 200 mm setup. Across a distance of approximately 140 mm the ring diameter will change from 3.75 mm to 2.89 mm. The gray shaded area indicates the position of the IIP based on the minimum in figure 4.8.

equivalent to that of [13] should suffice, i.e. a length of 70 µm and a diameter of $d_{\mathrm{ring,IP}} = 35\,\mu\mathrm{m}$. Furthermore, in order to fully characterize the optical dipole trap and its ability to confine the ^{39}K atoms, a camera calibration is needed, before an estimate of the trap depth in real units can be given.

The section is structured as follows. First a description of the camera calibration. Then a presentation of the different imaging systems, that were tested in the laboratory, used to achieve the diameter of $d_{\mathrm{ring,IP}}$, is provided. Finally, an estimate of the trap depth for the 200 mm-setup is given, based on the camera calibration and the demagnification of the imaging system.

4.2.1 Camera Calibration

Up until now, the depth of the generated ring potential was characterized by the camera's pixel values. However, a pixel value is not very telling, so a conversion is needed in order to get units, which are actual dipole potential depths that the atoms perceive e.g. in units of trapping temperature. To do this conversion, a camera calibration is needed. The relation between the total number of pixel count values and power is given by

$$C_{\mathrm{tot}} = P \cdot t_{\mathrm{exp}} \cdot \alpha, \tag{4.1}$$

where C_{tot} is the total number of pixel count values, i.e. the sum of each pixel's value. P is the power measured by a power meter after the optical fiber. The exposure time of the camera is t_{exp}, corresponding to the time the CMOS sensor is open for collecting photons. Finally, we have the conversion factor α, whose units will be in pixel values per Joule, and constitutes the factor we are looking for. The calibration was done, using a captured picture of the beam just after the out-coupler lens, seen on the left in figure 4.10.

To get the best possible calibration, the intensity of the beam is set such that the camera is not saturated. If a camera calibration is made with a saturated image, the pixels that are saturated do not yield the true pixel value and the calibration will be incorrect. This can be prevented either by turning down the power of the laser, or by dumping some of the intensity by using the PBS-waveplate configuration as shown in figure 3.4. The latter option is, without doubt, the best way since the laser operates in a steady state at the maximum current, and thus intensity fluctuations can be prevented. The number of pixels as a function of pixel values can be plotted in a histogram, shown on the right in figure 4.10. With the histogram at hand, the C_{tot} value in equation (4.1) can be found by taking the sum over all pixels. All the known factors can then be inserted in equation (4.1) and solved for α which yields $\alpha = 2.3612 \times 10^{16}$ PV/J where PV stands for pixel value. The α factor is all that is needed, to use the

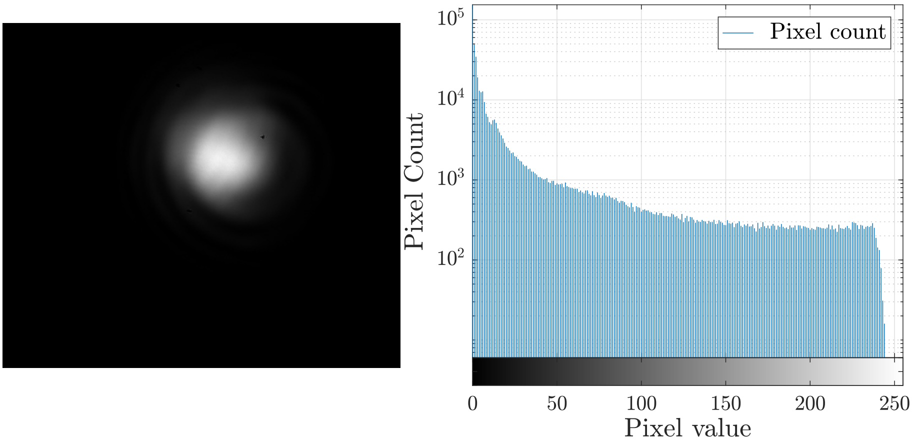

Figure 4.10: Left: Captured image of the Gaussian beam right after the out-coupler lens. Small impurities due to dust particles on the camera chip can be seen. This calibration image was taken with an exposure time of $t_{\text{exp}} = 0.1978 \times 10^{-3}$ s and a power measured by the power meter of $P = 2.5\,\mu\text{W}$. Right: Histogram showing the pixel distribution of the calibration image. It is of no surprise, that the majority of the pixels have a low pixel value since the beam only covers part of the CMOS chip. Also note, that no pixel value of 255 is present, meaning that the image was non-saturated.

camera as a power meter, which is the first step in order to get a real estimate of the generated dipole potential. To test whether our camera calibration works as intended, several images were taken where the power obtained from the camera was extracted and compared with the power meter, which ideally should be the same. The result can be seen in figure 4.11.

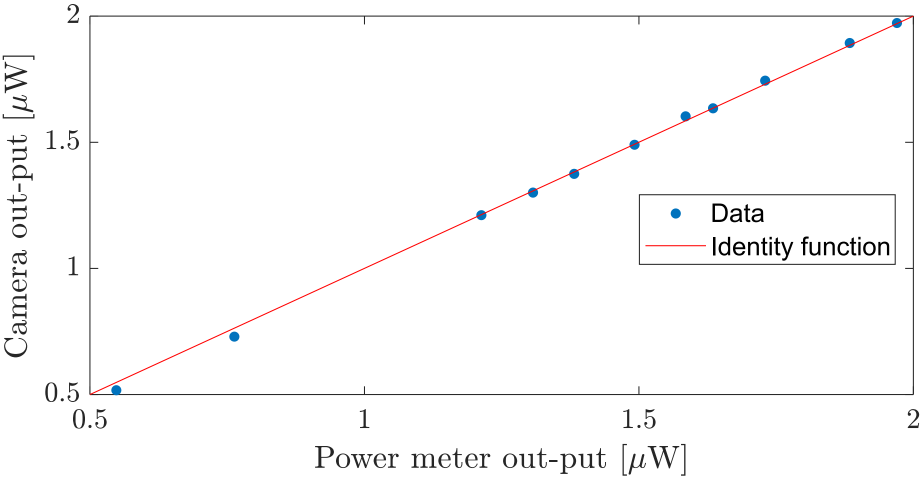

Figure 4.11: A plot showing the power obtained from the camera with the use of α, as a function of power measured by a power meter. The identity function is also plotted.

4.2.2 Imaging System

The ring-shaped intensity distribution can be imaged onto the atom sample by various optical setups.

The simplest way would be an imaging system consisting of two lenses which constitutes a Keplerian telescope. The telescope should then be orientated, such that the objective, i.e. the lens with the longest focal length f_1, is placed close to the IIP. The objective will then focus the collimated ring beam to an intermediary focus point at a distance f_1. The second lens, often called the eyepiece, is placed exactly at its corresponding focal length f_2 away from f_1, such that the separation between the two lenses is $f_1 + f_2$, creating what is called an afocal system, i.e. a system without focus and where no net convergence or divergence of the beam occurs. The magnification, or rather demagnification of the beam in this case, at the image plane (IP) will then be given by the simple formula

$M = \frac{f_2}{f_1}$. One of the issues that arise with such an imaging setup, is the limitation on the magnification. For instance, if we take the diameter of the ring in the 200 mm setup obtained in figure 4.4, which yielded $d_{\mathrm{ring,IIP}} = 3.033\,\mathrm{mm}$, the required demagnification would be about an 80-fold to get the diameter of $d_{\mathrm{ring,IP}}$. To construct a Keplerian telescope with this magnification power, would not be feasible in practice due to both aberration and diffraction effects. A setup with a 10-fold demagnification was tested in the laboratory for understanding purposes. It was realized by using an objective with $f_1 = 400\,\mathrm{mm}$, and an eyepiece of $f_2 = 40\,\mathrm{mm}$. Unfortunately, it was challenging to do any data-analysis and ring characterization, due to the relatively large pixel size of the IDS camera. A visualization of this issue is provided in figure 4.12. Both panels show a color image of the ring through two different imaging systems. The one on the left shows the ring through the Keplerian telescope system. Although the ring is captured in the vicinity of the image plane, it is clear, that the image is suffering from pixelation. The ring to the right in figure 4.12 is taken after a telescope-microscope configuration that will be described now.

A more sophisticated method of imaging would be to use a microscope objective in combination with a telescope. A proper microscope objective would make it possible to reach the 80-fold demagnification with reduced aberration and diffraction effects. Different in-house microscope objectives were tested during this project, and in particular one from ZEISS with an NA = 0.25 and a focal length of $f_{\mathrm{M,obj}} = 16.5\,\mathrm{mm}$ was of interest. With the known focal length of the microscope objective, the required effective focal length (EFL) of the telescope must be $f_{\mathrm{tele,EFL}} = 1320\,\mathrm{mm}$, to reach the 80-fold demagnification. OSLO was used to find the necessary lens combination, that gives this specific EFL, while making sure that the ring diameter after the telescope did not exceed the entrance pupil diameter of the microscope objective, which is given by $\text{Ø} = 2 \cdot \mathrm{NA} \cdot f_{\mathrm{M,obj}} = 8.25\,\mathrm{mm}$. These requirements were

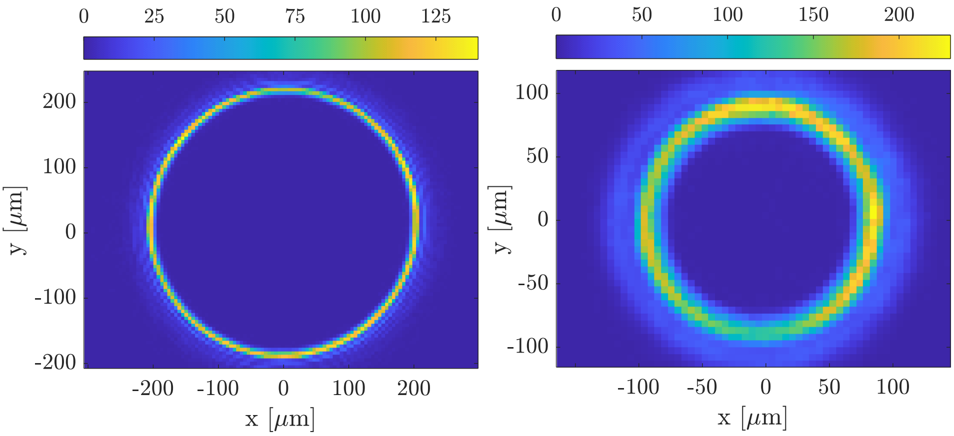

Figure 4.12: Left: Color image of the ring for the 200 mm setup through the Keplerian telescope with a 10-fold demagnification. Right: Color image of the ring for the 200 mm setup through the telescope - microscope configuration yielding a demagnification of 80. Note that this image is not taken at the image plane and therefore an out-of-focus ring is seen.

met by an achromatic doublet, with $f_{\text{tele},1}$ = 125 mm together with another achromatic doublet with $f_{\text{tele},2}$ = 400 mm separated by a distance of 479 mm from each other on the optical axis. After the beam paves through the microscope objective, an image appears in the vicinity of the focal plane of the objective. It is however unavoidable to have variations in the diameter of the ring across the trap length since the beam first converges and then diverges after the focal point. A sketch of the trap shape can be seen in figure 4.13, where it is obvious that the trap is not a perfect cylinder but resembles that of a conical frustum. In the right panel of figure 4.12 a resolvable color image of the ring captured after the focal point of the microscope objective can be seen.

Although the ring characteristics cannot be investigated just by placing the camera at the IP, the diameter variation across the trap can be

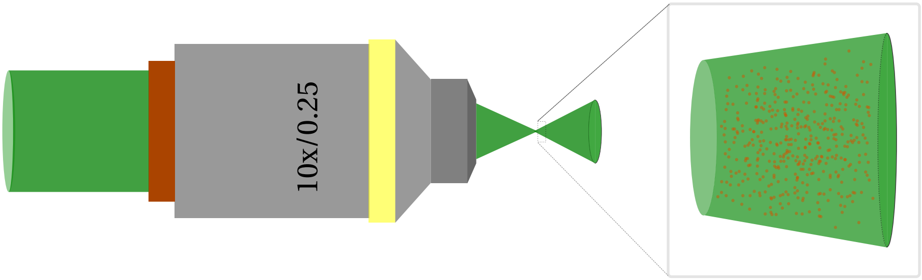

Figure 4.13: A ring beam enters the microscope objective and is imaged onto the atom sample. The inset shows the expected shape of the trap near the image plane with trapped atoms in it (orange dots).

estimated, by assuming that the ring beam expands linearly after the focal point. Measurements of the diameter of the ring at different z-positions, where the ring can be resolved, can be used to determine the divergence of the ring, and thus give an idea of the diameter variation along the trap. The linear fit yielded a slope equal to $a = 0.4789(17)$, hence for a trap length of 70 µm the diameter of the ring will vary up to 33.5 µm. This means we can expect almost a doubling of the diameter from one to the other end of the trap, with this type of microscope objective and imaging system.

4.2.3 Trap depth

To convert the units in figure 4.5 into units of trapping temperature, a few more steps need to be taken: First, the intensity in the equation of the dipole potential (2.26), can be found by converting the pixel values to a power, and then divided with the area of one pixel which is $A_{\text{pixel}} = (5.3\,\mu\text{m})^2$. Secondly, the relevant transition frequency that is needed in order to calculate the depth of the dipole potential, is given in appendix B figure B.1 for ^{39}K. Since we are using a laser with a detuning far greater than the fine-structure splitting of the P-state, we can treat the system as a simple two-level system with an $S \to P$ transition and take the transition frequency to be the mean value of the D_1 and D_2 line. We are now in a position where we can calculate the trap depth at the IIP. However, what is really interesting is the trap depth at the image plane where the atoms are located. Unfortunately, as mentioned earlier, the camera resolution is not high enough to resolve the ring at an 80-fold demagnification. Furthermore, the camera pixels tend to get saturated if a laser power above 3 µW is used in the 200 mm-setup. Two assumptions must be made to work around these issues. We can use the image taken at the IIP, and simply assume that we can apply an 80-fold demagnification to this image without losing any intensity. This means, we can divide the values we have on the x-axis in figure 4.5 with 80, and multiply the intensity with a factor of 80^2. In [13] they report that the total laser light reaching the atoms has a power of 700 mW. If we assume that our laser can provide similar power, we can scale up the power with a factor of 700 mW/3 µW. The resulting trap depth is presented in figure 4.14, with a 20-degree polynomial fit.

If we were to take this potential depth for granted, a trap depth of 150 µK would be more than enough to confine the atoms. This would make evaporative cooling highly suitable by lowering the intensity of the laser beam, thus letting the hottest atoms escape the trap and effectively cooling the remaining potassium atoms.

The 20-degree polynomial fit made in figure 4.14, can now be used to model the potential that the atoms feel. By inserting it into GPELab, we can simulate how the expected atom density distribution looks like. The scattering length is set to $a = 100a_0$, and the characteristic trap length is $L_{\text{trap}} = 1\,\mu\text{m}$. The result can be seen in figure 4.15 for different atom numbers in the trap, together with a plot of the trapping potential based on the fit from figure 4.14. Note that the GP Eq. (2.9) was rewritten, such that it is dimensionless, before it is defined in GPELab. That is why no units appear on the vertical axis on the plot of the trapping potential.

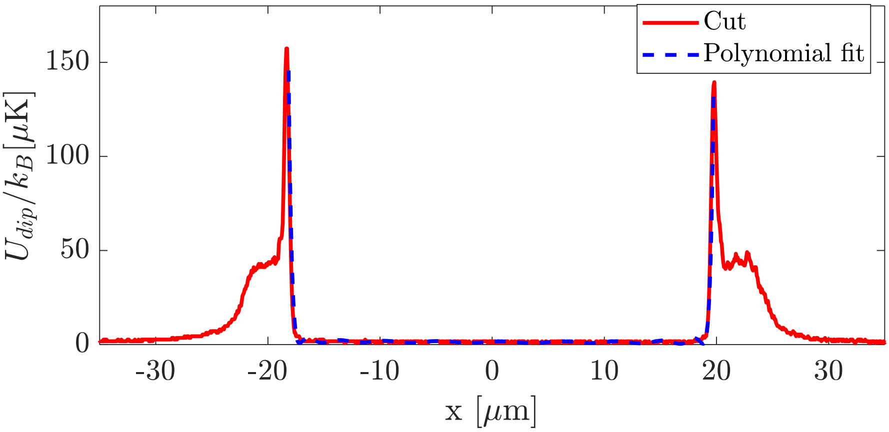

Figure 4.14: Trap depth profile of the 200 mm-setup based on the cut shown in figure 4.4. Two assumptions have been made to produce this figure: A demagnification of 80, and a laser power of 700 mW. A polynomial fit of degree 20 is fitted to the values in between the two inner peaks of the potential.

The characteristic plateaus of constant atom densities can be seen for atom numbers higher than $N = 10^3$. Due to the finite steepness of our potential, the atom density distribution shows longer wings, and thus longer healing lengths compared to the ideal box potential presented back in figure 2.2.

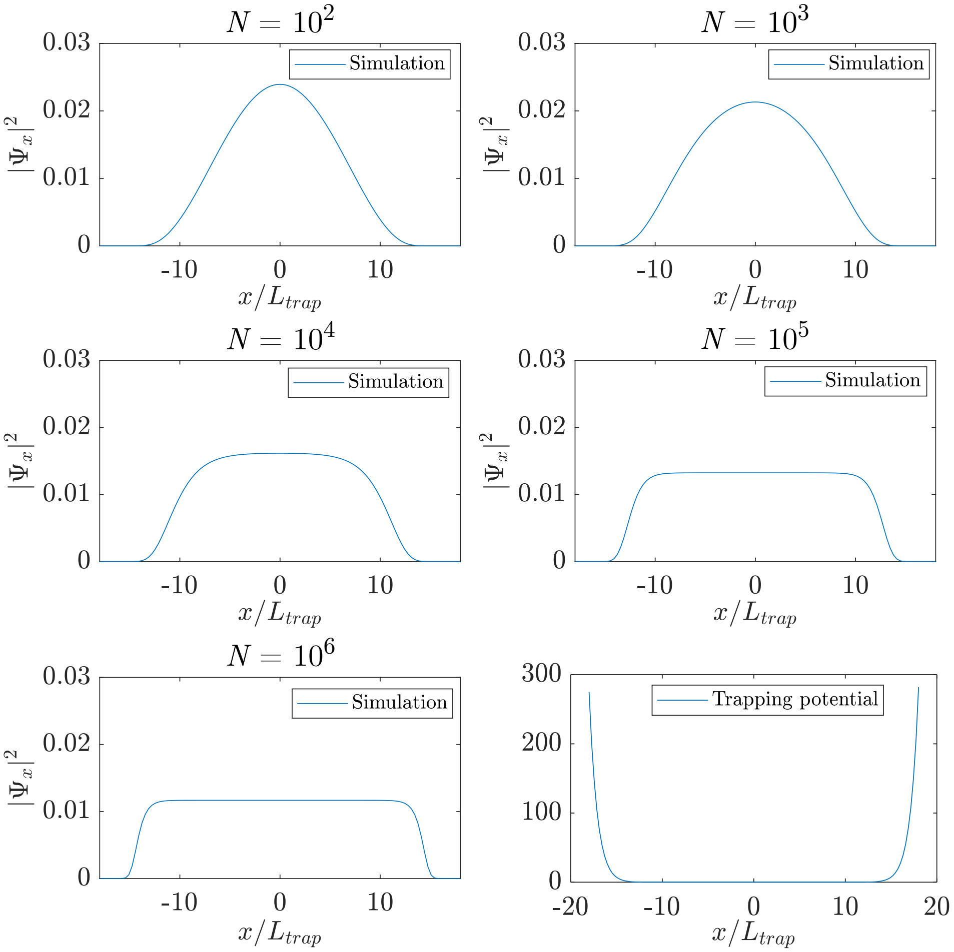

Figure 4.15: GPELab simulations of N-particles in a potential based on the 20-degree polynomial fit in figure 4.14. The resulting trapping potential defined in GPELab is also shown.

CHAPTER 5

CONCLUSION AND OUTLOOK

Within this thesis, the construction and characterization of a repulsive ring beam has been presented, with the intention of realizing an optical dipole trap for investigating impurity dynamics of ultracold gases.

At the beginning of my work (September 2020), I spend some time trying to get familiar with the experimental apparatus in MIX-lab used to produce ^{87}Rb and ^{39}K BECs. My work then continued in a separate laboratory where the ultimate goal was to build an optical system that could deliver a hollow repulsive light beam, and thus realize a blue detuned box potential for the atoms in MIX-lab. This was achieved in two different setups. First, a lens configuration inspired by the setup in [15] was realized and named the 400 mm setup. Due to poor performance and large diffraction effects, another setup was designed based on results from ray tracing simulations. When it comes to diffraction and aberration effects, the new self-designed system called the 200 mm setup showed promising results both in the laboratory and in simulations. The primary evaluation criterion for a repulsive optical dipole trap is the steepness of the walls when a cross-sectional cut is made. The 200 mm setup yielded a wall intensity that followed a power law given by $I(x) \propto x^{60.3(34)}$, thus greatly exceeding what was achieved with the 400 mm setup, i.e. $I(x) \propto x^{14.91(32)}$. Beside steep walls, one of the main merits of the two setups was the absent residual light within the ring potential, and thus not requiring an opaque mask. This allowed for an easy diameter change of the ring by simply varying the position of the last axicon. Furthermore, the setups also proved to be extremely power efficient since the majority of the intensity was distributed to the inner ring, and no power was dumped into an aperture stop. This became clear when the trap depth of the 200 mm setup was presented, yielding a trap depth of approximately 150 µK at a total laser power of 700 mW. Unfortunately, due to the resolution limitations of the camera, it was not possible to obtain the real trap depth through the imaging system, thus assumptions had to be made in order to calculate the trap depth at the image plane.

5.1 Outlook

Based on the results presented in this thesis, there are still a few things that need to be addressed before the final repulsive optical dipole trap can be implemented.

One of the main concerns regarding the imaging system, whose task is to take the image of the ring at the intermediate image plane and project it onto the atoms, is the resulting trap shape. A conical frustum with a diameter difference of 2 from one end to the other is not ideal. This could possibly be solved by substituting the microscope objective with an objective of longer focal length, since this would help to reduce the divergence of the ring after the focal point. Small variations in the diameter across the trap will however be inevitable using this type of imaging system.

In addition to the radial cylinder-shaped trap that was presented, sharp end cap walls are also needed to confine the atoms in the axial direction. One way to create these end caps could be by using a spatial light modulator [13], which shapes the incoming Gaussian beam and produces two outgoing sheet beams deflected in different directions, and then redirected onto the atoms orthogonal to the cylinder-shaped beam.

Finally, a proper laser with the capability of delivering high enough power to yield the necessary trap depth is also on the list of future implementations. This should however be relatively straightforward to realize since an AzurLight laser (10 W of 532 nm) is already bought and ready to use.

To summarize, the results presented in this thesis open up for intriguing opportunities to study quantum impurities without being limited by broadening effects caused by inhomogeneous atom density distributions.

Appendix A

Surface data spreadsheet

The surface data spreadsheet for the 200 mm and 400 mm setup in OSLO. All units are in millimeters.

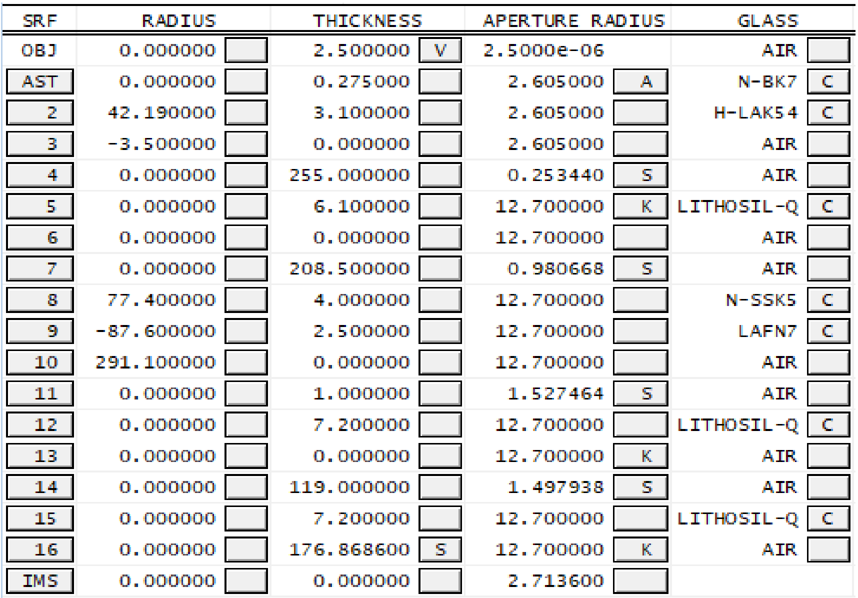

SRF	RADIUS		THICKNESS		APERTURE RADIUS		GLASS	
OBJ	0.000000		2.500000	V	2.5000e-06		AIR	
AST	0.000000		0.275000		2.605000	A	N-BK7	C
2	42.190000		3.100000		2.605000		H-LAK54	C
3	-3.500000		0.000000		2.605000		AIR	
4	0.000000		255.000000		0.253440	S	AIR	
5	0.000000		6.100000		12.700000	K	LITHOSIL-Q	C
6	0.000000		0.000000		12.700000		AIR	
7	0.000000		208.500000		0.980668	S	AIR	
8	77.400000		4.000000		12.700000		N-SSK5	C
9	-87.600000		2.500000		12.700000		LAFN7	C
10	291.100000		0.000000		12.700000		AIR	
11	0.000000		1.000000		1.527464	S	AIR	
12	0.000000		7.200000		12.700000		LITHOSIL-Q	C
13	0.000000		0.000000		12.700000	K	AIR	
14	0.000000		119.000000		1.497938	S	AIR	
15	0.000000		7.200000		12.700000		LITHOSIL-Q	C
16	0.000000		176.868600	S	12.700000	K	AIR	
IMS	0.000000		0.000000		2.713600			

Figure A.1: Surface data for the 200 mm setup

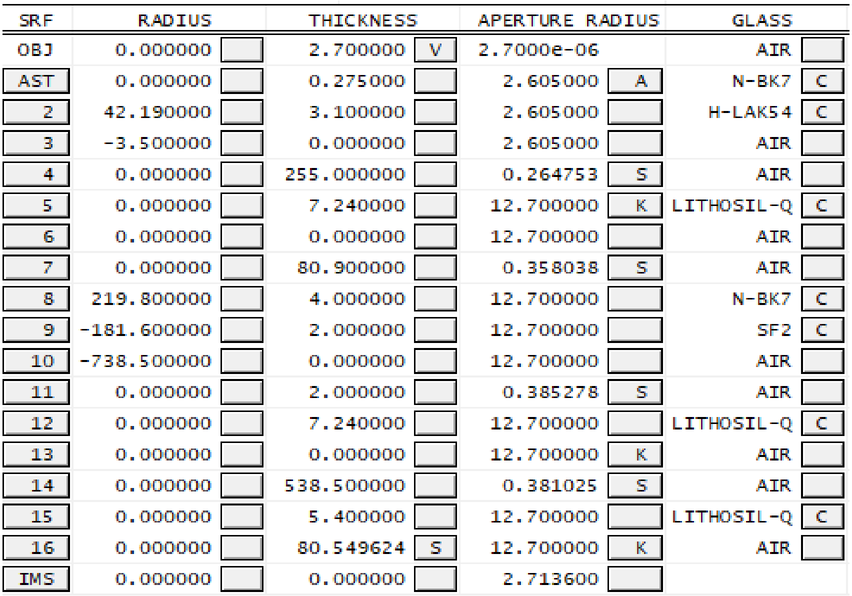

SRF	RADIUS		THICKNESS		APERTURE RADIUS		GLASS	
OBJ	0.000000		2.700000	V	2.7000e-06		AIR	
AST	0.000000		0.275000		2.605000	A	N-BK7	C
2	42.190000		3.100000		2.605000		H-LAK54	C
3	-3.500000		0.000000		2.605000		AIR	
4	0.000000		255.000000		0.264753	S	AIR	
5	0.000000		7.240000		12.700000	K	LITHOSIL-Q	C
6	0.000000		0.000000		12.700000		AIR	
7	0.000000		80.900000		0.358038	S	AIR	
8	219.800000		4.000000		12.700000		N-BK7	C
9	-181.600000		2.000000		12.700000		SF2	C
10	-738.500000		0.000000		12.700000		AIR	
11	0.000000		2.000000		0.385278	S	AIR	
12	0.000000		7.240000		12.700000		LITHOSIL-Q	C
13	0.000000		0.000000		12.700000	K	AIR	
14	0.000000		538.500000		0.381025	S	AIR	
15	0.000000		5.400000		12.700000		LITHOSIL-Q	C
16	0.000000		80.549624	S	12.700000	K	AIR	
IMS	0.000000		0.000000		2.713600			

Figure A.2: Surface data for the 400 mm setup

Appendix B

Energy diagram of Potassium-39

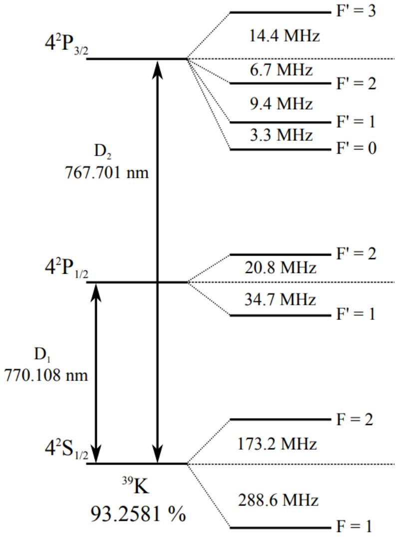

Figure B.1: An energy level diagram of the 4S → 4P D lines of ^{39}K. Both the fine structure- and hyperfine structure splitting are depicted. Reprinted from [38].

BIBLIOGRAPHY

[1] R. Wesche, Superconductivity: A Macroscopic Quantum Phenomenon, in *Physical properties of high-temperature superconductors* (Wiley, May 2015), pp. 45–68.

[2] Y. Imry, On macroscopic quantum phenomena associated with the quantised Hall effect, Journal of Physics C: Solid State Physics **16**, 3501–3511 (1983).

[3] A. Einstein, Quantentheorie des einatomigen idealen gases: zweite abhandlung, Sitzungber. Kgl. Akad. Wiss. (1925).

[4] S. N. Bose, Plancks Gesetz und Lichtquantenhypothese, Zeitschrift für Physik **26**, 178–181 (1924).

[5] M. H. Anderson, J. R. Ensher, M. R. Matthews, C. E. Wieman and E. A. Cornell, Observation of Bose-Einstein Condensation in a Dilute Atomic Vapor, Science **269**, 198 LP –201 (1995).

[6] J. R. Abo-Shaeer, C. Raman, J. M. Vogels and W. Ketterle, Observation of Vortex Lattices in Bose-Einstein Condensates, Science **292**, 476 LP –479 (2001).

[7] I. Bloch, T. W. Hänsch and T. Esslinger, Measurement of the spatial coherence of a trapped Bose gas at the phase transition, Nature **403**, 166–170 (2000).

[8] D. Hellweg, L. Cacciapuoti, M. Kottke, T. Schulte, K. Sengstock, W. Ertmer and J. J. Arlt, Measurement of the Spatial Correlation Function of Phase Fluctuating Bose-Einstein Condensates, Physical Review Letters **91**, 10406 (2003).

[9] M. G. Skou, T. G. Skov, N. B. Jørgensen, K. K. Nielsen, A. Camacho-Guardian, T. Pohl, G. M. Bruun and J. J. Arlt, Non-equilibrium quantum dynamics and formation of the Bose polaron, Nature Physics, `10.1038/s41567-021-01184-5` (2021).

[10] A. Camacho-Guardian, L. A. Pena Ardila, T. Pohl and G. M. Bruun, Bipolarons in a Bose-Einstein Condensate, Physical Review Letters **121**, 13401 (2018).

[11] L. J. Wacker, Few-body physics with ultracold potassium rubidium mixtures, PhD thesis (Aarhus University, 2015).

[12] N. B. Jørgensen, L. Wacker, K. T. Skalmstang, M. M. Parish, J. Levinsen, R. S. Christensen, G. M. Bruun and J. J. Arlt, Observation of Attractive and Repulsive Polarons in a Bose-Einstein Condensate, Physical Review Letters **117**, 55302 (2016).

[13] A. L. Gaunt, T. F. Schmidutz, I. Gotlibovych, R. P. Smith and Z. Hadzibabic, Bose-Einstein Condensation of Atoms in a Uniform Potential, Physical Review Letters **110**, 200406 (2013).

[14] B. Mukherjee, Z. Yan, P. B. Patel, Z. Hadzibabic, T. Yefsah, J. Struck and M. W. Zwierlein, Homogeneous Atomic Fermi Gases, Physical Review Letters **118**, 123401 (2017).

[15] K. Hueck, N. Luick, L. Sobirey, J. Siegl, T. Lompe and H. Moritz, Two-Dimensional Homogeneous Fermi Gases, Physical Review Letters **120**, 60402 (2018).

[16] C. J. Pethick and H. Smith, Bose–Einstein Condensation in Dilute Gases, 2nd ed. (Cambridge University Press, Cambridge, 2008).

[17] C. J. Foot, Atomic physics, Oxford master series in atomic, optical, and laser physics (Oxford University Press, Oxford, 2007).

[18] X. Antoine and R. Duboscq, GPELab, a Matlab toolbox to solve Gross–Pitaevskii equations I: Computation of stationary solutions, Computer Physics Communications **185**, 2969–2991 (2014).

[19] X. Antoine and R. Duboscq, Robust and efficient preconditioned Krylov spectral solvers for computing the ground states of fast rotating and strongly interacting Bose–Einstein condensates, Journal of Computational Physics **258**, 509–523 (2014).

[20] D. J. Griffiths and D. F. Schroeter, Introduction to Quantum Mechanics, 3rd ed. (Cambridge University Press, Cambridge, 2018).

[21] M. Lysebo and L. Veseth, Feshbach resonances and transition rates for cold homonuclear collisions between K39 and K41 atoms, Physical Review A - Atomic, Molecular, and Optical Physics **81**, 32702 (2010).

[22] E. Timmermans, P. Tommasini, M. Hussein and A. Kerman, Feshbach resonances in atomic Bose–Einstein condensates, Physics Reports **315**, 199–230 (1999).

[23] C. Chin, R. Grimm, P. Julienne and E. Tiesinga, Feshbach resonances in ultracold gases, Reviews of Modern Physics **82**, 1225–1286 (2010).

[24] R. Blatt and D. Wineland, Entangled states of trapped atomic ions, Nature **453**, 1008–1015 (2008).

[25] R. Grimm, M. Weidemüller and Y. B. Ovchinnikov, Optical Dipole Traps for Neutral Atoms, in , Vol. 42, edited by B. Bederson, W. Molecular and H. B. T. A. I. A. Optical Physics (Academic Press, 2000), pp. 95–170.

[26] D. A. Steck, *Quantum and atom optics*, `https://atomoptics-nas.uoregon.edu/~dsteck/teaching/quantum-optics/quantum-optics-notes.pdf`, 2007.

[27] J. H. McLeod, The Axicon: A New Type of Optical Element, Journal of the Optical Society of America **44**, 592–597 (1954).

[28] E. O. Inc., *An in-depth look at axicons*, `https://www.edmundoptics.com/knowledge-center/application-notes/lasers/an-in-depth-look-at-axicons/`, Accessed: 2021-03-05.

[29] B. Dépret, P. Verkerk and D. Hennequin, Characterization and modelling of the hollow beam produced by a real conical lens, Optics Communications **211**, 31–38 (2002).

[30] K. M. Hueck, A homogeneous, two-dimensional fermi gas, PhD thesis (University of Hamburg, June 2017).

[31] N. Corporation, *Fiber optic basics*, `https://www.newport.com/t/fiber-optic-basics`, Accessed: 2021-04-05.

[32] C. Pruss, E. Garbusi and W. Osten, Testing Aspheres, Optics & Photonics News **19**, 24 (2008).

[33] *Optalix reference manual*, Optenso (Aug. 2020).

[34] E. Hecht, Optics (Pearson Education, Incorporated, 2017).

[35] *Oslo optics reference*, Lambda Research Corporation (2011).

[36] *Oslo user manual guide*, Lambda Research Corporation (Mar. 2021).

[37] IDS, *Ui-1240se-nir-gl*, `https://en.ids-imaging.com/store/ui-1240se.html`, Accessed: 2021-06-15.

[38] R. K. Hanley, P. D. Gregory, I. G. Hughes and S. L. Cornish, Absolute absorption on the potassium D lines: theory and experiment, Journal of Physics B: Atomic, Molecular and Optical Physics **48**, 195004 (2015).